Published for SISSA by Springer

Received: *February 10, 2017*
Revised: *June 22, 2017*
Accepted: *July 10, 2017*
Published: *August 1, 2017*

Directions for model building from asymptotic safety

Andrew D. Bond,[a] **Gudrun Hiller,**[b] **Kamila Kowalska**[b] **and Daniel F. Litim**[a]

[a] *Department of Physics and Astronomy, University of Sussex, Brighton, BN19QH, United Kingdom*
[b] *Institut für Physik, Technische Universität Dortmund, D-44221 Dortmund, Germany*

E-mail: a.bond@sussex.ac.uk, gudrun.hiller@uni-dortmund.de, kamila.kowalska@tu-dortmund.de, d.litim@sussex.ac.uk

Abstract: Building on recent advances in the understanding of gauge-Yukawa theories we explore possibilities to UV-complete the Standard Model in an asymptotically safe manner. Minimal extensions are based on a large flavor sector of additional fermions coupled to a scalar singlet matrix field. We find that asymptotic safety requires fermions in higher representations of $\mathrm{SU}(3)_C \times \mathrm{SU}(2)_L$. Possible signatures at colliders are worked out and include R-hadron searches, diboson signatures and the evolution of the strong and weak coupling constants.

Keywords: Beyond Standard Model, Perturbative QCD, Renormalization Group

ArXiv ePrint: 1702.01727

https://doi.org/10.1007/JHEP08(2017)004

Contents

JHEP08(2017)004

1 Introduction

Asymptotic freedom plays a central role in the construction of the Standard Model (SM) of particle physics and extensions thereof [1, 2]. It predicts that interactions are dynamically switched off at highest energies due to quantum fluctuations. In the language of the renormalisation group, asymptotic freedom corresponds to a free ultraviolet (UV) fixed point. Asymptotic freedom famously requires the presence of non-abelian gauge fields [3], together with suitable matter interactions to ensure that Yukawa and scalar couplings reach the free fixed point in the UV alongside the non abelian gauge coupling [4]. Identifying viable theories beyond the Standard Model (BSM) with complete asymptotic freedom continues to be an active area of research [5–7].

Asymptotic safety states that fundamental quantum fields may very well remain interacting at highest energies [8, 9], implying that running couplings reach an interacting (rather than a free) UV fixed point under the renormalisation group evolution. If so, theories remain well-behaved and predictive up to highest energies in close analogy to theories with complete asymptotic freedom. Asymptotic safety has initially been put forward as a scenario for quantum gravity [9] where a large amount of evidence has arisen from increasingly sophisticated studies in four dimensions including signatures at colliders (see [10] for an overview). More recently, necessary and sufficient conditions for asymptotic safety in general weakly coupled gauge theories (without gravity) have been derived, alongside strict no go theorems [11]. Most importantly, it was found that Yukawa interactions together with elementary scalar fields such as the Higgs offer a unique key towards asymptotic safety [11]. Moreover, an important proof of existence has been provided in [12], and further expanded in [13], showing that exact asymptotic safety with a stable ground state can arise in SU(N) gauge theories under strict perturbative control in the Veneziano limit. The feasibility of asymptotic safety is thus well motivated theoretically and opens intriguing new directions for model building beyond the SM.

In this paper, we make a first step to investigate asymptotically safe extensions of the SM and phenomenological signatures thereof at colliders. Our motivation for doing so is twofold. Firstly, we want to understand whether and how minimal extensions of the SM can be found with weakly interacting UV fixed points. We are particularly interested in the "phase space" of such extensions, and in the concrete conditions under which interacting UV fixed points are connected through well-defined trajectories with the SM at low energies. Secondly, we wish to understand how phenomenological constraints may arise through existing data, and, more generally, the conditions under which asymptotic safety can be tested at colliders. Our investigation is "top-down" in that we begin by requiring conditions under which weakly coupled asymptotic safety can be achieved. Our central new input are BSM fermions and scalars, some of which are charged under the gauge symmetries of the SM. Our approach will be minimal in that we add a single BSM Yukawa coupling whose sole task is to negotiate asymptotically safe UV completions for the SM with $\mathrm{SU}(3)_C \otimes \mathrm{SU}(2)_L \otimes \mathrm{U}(1)_Y$ gauge symmetry.

The paper has the following format. In section 2 we discuss the basic perturbative mechanism for asymptotic safety in gauge theories including general conditions for exis-

JHEP08(2017)004

tence. In section 3 we investigate minimal extensions of the Standard Model in view of weakly interacting high energy fixed points. In section 4, we explain the conditions under which interacting UV fixed points are connected with the SM at low energies. Phenomenological implications are worked out in section 5. We summarize in section 6. Appendix A contains technicalities summarising the perturbative loop coefficients and group theoretical information, and details of UV-IR connecting separatrices.

2 Basics of asymptotic safety for gauge theories

In this section, we recall the basic mechanism for asymptotic safety in four-dimensional gauge theories with matter and recall general theorems for asymptotic safety in weakly coupled gauge theories following [11, 12]. We also introduce some notation and conventions.

2.1 Weakly interacting UV fixed points

We begin with a discussion of asymptotic safety in gauge theories and the renormalisation group running of couplings. In the absence of asymptotic freedom, it is well-known that perturbative couplings would grow towards higher energies thereby limiting predictivity to a highest energy scale Λ. The main feature of asymptotic safety, however, is that the growth of couplings is tamed, dynamically, through a weakly interacting fixed point. An explicit mechanism which allows quantum fields to avoid the notorious Landau poles of QED-like theories has recently been discovered in [12]. Strict theorems for asymptotic safety in general weakly coupled gauge theories have been derived in [11].

To illustrate the mechanism, and to prepare for our models below, we consider the renormalization group (RG) flow for a simple gauge theory with gauge coupling $\alpha_g = g^2/(4\pi)^2$ interacting with scalars and fermions, with Yukawa coupling $\alpha_y = y^2/(4\pi)^2$. Within perturbation theory, the RG flow in the gauge-Yukawa system to the leading non-trivial order is given by

$$\begin{aligned} \beta_g &\equiv \frac{d\alpha_g}{d\ln\mu} = (-B + C\,\alpha_g - D\,\alpha_y)\,\alpha_g^2\,, \\ \beta_y &\equiv \frac{d\alpha_y}{d\ln\mu} = (E\,\alpha_y - F\,\alpha_g)\,\alpha_y\,. \end{aligned} \tag{2.1}$$

Scalar selfcouplings do not impact on interacting fixed points to leading order at weak coupling and can be neglected. The various loop coefficients B, C, D, E and F depend on the matter content of the theory, which we leave unspecified at this stage. The gauge coupling is asymptotically free (infrared free) provided that the one loop gauge coefficient obeys $B > 0$ ($B < 0$). The two loop gauge coefficient C may take either sign depending on the matter content. Provided that asymptotic freedom is absent, $B < 0$, it has also been shown that $C > 0$ [11]. The other loop coefficients obey $D, E, F > 0$ for any quantum field theory, irrespective of the matter content. Also notice that Yukawa couplings always contribute with a negative sign to the running of the gauge coupling, irrespective of the sign of B.

JHEP08(2017)004

In general, theories with (2.1) may have various types of fixed points, depending on the matter content. Equating $\beta_i = 0$ for both couplings, three types of fixed points are found. The Gaussian fixed point

$$(\alpha_g^*, \alpha_y^*) = (0, 0) \tag{2.2}$$

always exists, and corresponds to the UV (IR) fixed point provided that $B > 0$ ($B < 0$). An interacting fixed point where Yukawa interactions are switched-off may also exist, with

$$(\alpha_g^*, \alpha_y^*) = \left(\frac{B}{C}, 0\right). \tag{2.3}$$

This is the well-known Caswell-Banks-Zaks fixed point [14, 15] which requires $B \cdot C > 0$ to be physical and $B/C \ll 1$ to be perturbative. It is also known that $B \cdot C < 0$ as soon as $B < 0$ for any quantum field theory [11]. This result has the form of a no go theorem: in four dimensions, weakly coupled gauge theories cannot become asymptotically safe without Yukawa interactions. Hence, Caswell-Banks-Zaks fixed points (2.3) are invariably IR fixed points.

A fully interacting gauge-Yukawa fixed point may arise provided that the Yukawa coupling is non-vanishing. Requiring $\beta_y = 0$, (2.1) implies that the gauge and Yukawa coupling are proportional to each other, $\alpha_y = \frac{F}{E}\alpha_g$. This nullcline condition modifies the running of the gauge coupling and turns (2.1) into

$$\beta_g = (-B + C'\,\alpha_g)\,\alpha_g^2\,, \tag{2.4}$$

where the two loop term is effectively shifted $C \to C'$ owing to Yukawa interactions, with

$$C' = C - D\frac{F}{E} < C\,. \tag{2.5}$$

This shift term has important implications: firstly, the fixed point is now fully interacting, with the gauge coupling taking the form (2.3) with C shifted as in (2.5), together with the interacting fixed point for the Yukawa coupling,

$$(\alpha_g^*\,, \alpha_y^*) = \left(\frac{B}{C'}\,, \frac{B}{C'}\frac{F}{E}\right). \tag{2.6}$$

Secondly, for theories with asymptotic freedom ($B > 0$), and provided that $C' > 0$, the gauge-Yukawa fixed point (2.6) corresponds to an IR fixed point. It can be reached by RG trajectories emanating out of the Gaussian UV fixed point. Finally, for theories without asymptotic freedom ($B < 0$) the gauge coupling may now take a viable interacting fixed point $\alpha_g^* = B/C' > 0$ as long as $C' < 0$. This is the interacting UV fixed point of asymptotic safety (see table 1 for a summary). The result is in stark contrast to theories without Yukawa interactions, where (2.3) cannot possibly become an UV fixed point. We conclude that the Yukawa interactions are of crucial importance for asymptotic safety [11]. Moreover, the necessary condition for asymptotic safety at weak coupling $B, C' < 0$, see table 1 **c)**, now translates into a simple condition relating the one and two loop coefficients appearing in (2.1),

$$C' < 0 \quad \Leftrightarrow \quad DF - CE > 0\,. \tag{2.7}$$

JHEP08(2017)004

Case	*Parameter*	*Fixed point*	*Info*	*Type*
a)	$B > 0$, $C > 0$	IR	asymptotic freedom	Caswell-Banks-Zaks (BZ)
b)	$B > 0$, $C' > 0$	IR	asymptotic freedom	gauge-Yukawa (GY)
c)	$B < 0$, $C' < 0$	UV	asymptotic safety	gauge-Yukawa (GY)

Table 1. All weakly interacting fixed points α_* of simple gauge theories with (2.1) and their dependence on the matter content expressed through the parameters B, C and C', see [11].

In the remaining part of the paper, we evaluate whether the condition (2.7) can be achieved for extensions of the SM.

2.2 Scaling behaviour

In the vicinity of a free (UV or IR) fixed point the running of couplings is logarithmically slow. In the vicinity of interacting (UV or IR) fixed points, instead, the running of couplings is power law like, characterised by universal scaling exponents $\{\vartheta_i\}$. Linearising the RG flow in the vicinity of a fixed point

$$\beta_i = \sum_j M_{ij} \, (\alpha_j - \alpha_j^*) + \text{subleading} \,, \tag{2.8}$$

the scaling exponents can be derived as the eigenvalues of the stability matrix $M_{ij} = \partial\beta_i/\partial\alpha_j|_*$. Eigendirections are termed relevant (irrelevant) provided that $\vartheta < 0$ ($\vartheta > 0$). Marginal couplings have vanishing eigenvalues at linear order (2.8), reflecting logarithmic running. Whether these are marginally relevant ($\vartheta = 0^-$) such as in QCD, or marginally irrelevant ($\vartheta = 0^+$) such as in QED, is determined beyond leading order. In the vicinity of interacting fixed points couplings scale according to

$$\alpha_i(\mu) = \alpha_i^* + \sum_n c_n V_i^n \left(\frac{\mu}{\mu_0}\right)^{\vartheta_n} + \text{subleading} \,, \tag{2.9}$$

where V^n are the eigenvectors of the stability matrix with eigenvalue ϑ_n, μ denotes the RG scale, and c_n are free numbers. The significance of (2.9) is as follows [16, 17]. In order to achieve a well-defined UV limit, the parameters c_n related to irrelevant eigenvalues must be set identically to zero, or else the UV fixed point cannot possibly be reached from (2.9) in the limit $\mu \to \infty$. On the other side, the relevant eigendirections are unconstrained and the corresponding numbers c_n are free parameters of the theory. Provided that the number of relevant directions is finite, the theory is predictive with a finite number of free parameters whose values must be determined by experiment.

Returning to the models at hand, three different types of interacting fixed points arise. At a Caswell-Banks-Zaks fixed point (2.3), scaling exponents are given by

$$\vartheta_1 = -BF/C \,, \tag{2.10}$$

$$\vartheta_2 = B^2/C \,, \tag{2.11}$$

JHEP08(2017)004

to leading order in $B/C \ll 1$, with $\vartheta_1 < 0 < \vartheta_2$. Consequently, the fixed point has a relevant direction corresponding to the Yukawa interaction, and an irrelevant one, corresponding to the gauge coupling, see table 1 **a)**. At the gauge-Yukawa fixed point (2.6), the scaling exponents of the theory are given by

$$\vartheta_1 = B^2/C' \,, \tag{2.12}$$

$$\vartheta_2 = BF/C' \,, \tag{2.13}$$

to leading order in $B/C' \ll 1$.[1] For asymptotically free theories, we note that $0 < \vartheta_1 < \vartheta_2$, meaning that both directions are IR attractive, see table 1 **b)**. In the remaining part of the paper we are particularly interested in theories with asymptotic safety where $B < 0$. For these, the eigenvalues are of the form $\vartheta_1 < 0 < \vartheta_2$, see table 1 **c)**. It states that the fixed point has a one dimensional UV critical surface characterised by the relevant direction given through ϑ_1 [12].

2.3 Theorems for asymptotic safety

General theorems for asymptotic safety in weakly coupled gauge theories have recently been derived in [11]. In particular, it has been established that Yukawa interactions offer a *unique* mechanism towards asymptotic safety. Neither gauge interactions nor scalar self interactions are able to negotiate an interacting UV fixed point at weak coupling. Stated differently, it is impossible to find an asymptotically safe and weakly coupled gauge theory with simple or product gauge groups but without Yukawa interactions. Hence, asymptotic safety in four dimensional gauge theories invariably requires elementary scalars and fermions, besides the gauge fields. Furthermore, fermions must minimally be charged under some or all of the gauge group(s). For general gauge theories with product gauge group $\mathcal{G} = \mathcal{G}_1 \otimes \mathcal{G}_2 \otimes \cdots \otimes \mathcal{G}_n$, weakly interacting fixed points arise as solutions to the linear equations [11]

$$B_i' = C_{ij}\, \alpha_j^* \,, \quad \text{subject to} \quad \alpha_j^* \geq 0 \,, \tag{2.14}$$

where C_{ij} denotes the matrix of two loop gauge contributions, and $B_i' = B_i + 2\, Y_{4,i}^*$ the one-loop coefficient shifted by the Yukawa terms $Y_{4,i}^* = \mathrm{Tr}[\mathbf{C}_2^{F_i}\, \mathbf{Y}_*^A\, (\mathbf{Y}_*^A)^\dagger]/d(G_i) \geq 0$ at the interacting fixed point. Here, $\mathbf{C}_2^{F_i}$ denotes the Casimir of the fermions, $\mathbf{Y}^A$ the matrix of Yukawa couplings, and $d(G_i)$ the dimension of the group G_i following the conventions of [18–21]. It has also been shown in [11] that for any infrared free gauge factor ($B_i < 0$), the necessary condition for asymptotic safety amongst the solutions to (2.14) is

$$B_i' > 0 \,. \tag{2.15}$$

It states that Yukawa interactions must effectively change the sign of the one loop coefficient for the infrared free gauge couplings, generalising the necessary condition (2.7) to general gauge theories. Sufficiency conditions for asymptotic safety, in addition to the mandatory presence of Yukawa couplings, have also been detailed in [11]. These relate to the specifics of the Yukawa sector as well as to the viability of the scalar sector including

[1] Notice that (2.12) and (2.13) do not follow from (2.10) and (2.11) by substituting $C \to C'$.

JHEP08(2017)004

the stability of the vacuum. It then remains to investigate whether the mandatory and sufficient conditions for asymptotic safety have viable weakly coupled UV fixed points as their solutions. In the remaining part of the paper, we investigate in concrete terms the availability of asymptotically safe solutions of (2.14), (2.15) for BSM extensions of the $\mathrm{SU}(3)_C \times \mathrm{SU}(2)_L$ sector of the SM.

3 Asymptotic safety beyond the Standard Model

In this section, we investigate minimal extensions of the SM and conditions under which asymptotic safety becomes available in the deep UV [11]. While designing the structure of the BSM sector, we make use of the properties of the gauge-Yukawa theory where asymptotic safety can be achieved by an interplay between the gauge and Yukawa interactions of vector-like fermions and a scalar matrix field [12].

3.1 Minimal BSM extensions

Asymptotic safety in BSM extensions minimally require the presence of new matter fields which carry charges under the SM gauge groups and thereby modify the RG running of couplings. Guided by the findings of [11, 12], we consider the existence of N_F flavors of BSM vector-like fermions ψ which minimally couple to the SM gauge bosons. In general, the BSM fermions may carry charges under $\mathrm{SU}(3)_C$, $\mathrm{SU}(2)_L$, or hypercharge Y, meaning

$$\psi_i(R_3, R_2, Y)\,, \tag{3.1}$$

where $i = 1, \cdots, N_F$ denotes the flavor index. Furthermore, the BSM fermions couple via Yukawa interactions to complex scalar fields S_{ij} which we take to be a singlet under the SM. Since the BSM fermions are taken to be vector-like, anomalies are not an issue. The Yukawa interactions are given by

$$L_{\text{BSM, Yukawa}} = -y\,\mathrm{Tr}(\overline{\psi}_L\, S\, \psi_R + \overline{\psi}_R\, S^\dagger\, \psi_L)\,. \tag{3.2}$$

Here, y denotes the BSM Yukawa coupling, the trace Tr sums over color and flavor indices, and the decomposition $\psi = \psi_L + \psi_R$ with $\psi_{R/L} = \frac{1}{2}(1 \pm \gamma_5)\psi$ is understood. Yukawa interactions are crucial for asymptotic safety to arise in weakly coupled gauge theories. The BSM sector is invariant under global $\mathrm{U}(N_F) \times \mathrm{U}(N_F)$ flavor rotations. The full Lagrangean for the BSM extension of the SM is given by

$$L = L_{\text{SM}} + L_{\text{BSM, kin.}} + L_{\text{BSM, pot.}} + L_{\text{BSM, Yukawa}}\,. \tag{3.3}$$

Here, L_{SM} denotes the SM Lagrangean and $L_{\text{BSM, pot.}}$ the interaction Lagrangean of the BSM scalars. The BSM scalars S can mix with the SM Higgs boson through suitable portal coupling contained in $L_{\text{BSM, pot.}}$. The BSM kinetic terms are given by

$$L_{\text{BSM, kin.}} = \mathrm{Tr}(\overline{\psi}\, i\not{D}\, \psi) + \mathrm{Tr}(\partial_\mu S^\dagger\, \partial^\mu S)\,. \tag{3.4}$$

The BSM fermions communicate to the SM through the gauge interactions, provided they are charged accordingly. The scalar fields are taken to be singlets under the SM gauge

JHEP08(2017)004

groups. We assume that the BSM matter fields develop soft scalar M_S and fermion M_ψ masses for the model to be compatible with data.

For the sake of this paper we make a few further simplifying assumptions. Firstly, we limit ourselves to BSM fermions which carry no hypercharge. This assumption can be relaxed without changing the overall picture of results. Secondly, we neglect the role of quartic self interactions of the BSM scalars as well as portal couplings to the Higgs. At weak coupling, neither of these are relevant for the primary existence of the UV fixed point in the gauge-Yukawa sector.[2] Consequently, the free fundamental parameters of the BSM matter sector are given by their group-theoretical representation under $\mathrm{SU}(2)_L$ and $\mathrm{SU}(3)_C$, and their flavor multiplicity N_F,

$$(R_2, R_3, N_F)\,. \tag{3.5}$$

A key goal of our study will be to identify viable, weakly coupled UV fixed points for the BSM theory (3.3) within the parameter space (3.5).

3.2 Renormalisation group

In order to identify interacting fixed points, we must analyse the RG equations for the theory (3.3). Within perturbation theory, weakly interacting fixed points arise for the first time at the two loop level in the gauge sector and at the one loop level in the Yukawa and scalar sectors [11]. Also, interacting UV fixed points necessarily require the presence of a fixed point in the Yukawa interactions. For these reasons, we consider the RG equations for (3.3) up to second order in both gauge couplings, and up to first order in the BSM Yukawa coupling. This is the lowest order at which a weakly coupled UV fixed point may arise.

To be concrete, we normalise the gauge and Yukawa couplings with the perturbative loop factor and introduce

$$\alpha_2 = \frac{g_2^2}{(4\pi)^2}\,, \qquad \alpha_3 = \frac{g_3^2}{(4\pi)^2}\,, \qquad \alpha_y = \frac{y^2}{(4\pi)^2}\,, \tag{3.6}$$

to denote the weak, strong, and BSM Yukawa coupling, respectively.[3] Our study will be confined to the perturbative domain where all couplings remain sufficiently small. For now, we use $\alpha < 1$ as a practitioner's criterion for weak coupling. We return to this aspect in section 4.5. In terms of (3.6), the RG equations within dimensional regularisation and to the leading non-trivial order are given by [18–21]

$$\begin{aligned}
\beta_3 &\equiv \frac{d\alpha_3}{d\ln\mu} = (-B_3 + C_3\,\alpha_3 + G_3\,\alpha_2 - D_3\,\alpha_y)\,\alpha_3^2\,,\\
\beta_2 &\equiv \frac{d\alpha_2}{d\ln\mu} = (-B_2 + C_2\,\alpha_2 + G_2\,\alpha_3 - D_2\,\alpha_y)\,\alpha_2^2\,,\\
\beta_y &\equiv \frac{d\alpha_y}{d\ln\mu} = (E\,\alpha_y - F_2\,\alpha_2 - F_3\,\alpha_3)\,\alpha_y\,.
\end{aligned} \tag{3.7}$$

[2] A detailed analysis of the SM Yukawa and scalar sector will be given elsewhere.

[3] Our definition for the gauge couplings relates to the more standard definition $\alpha_s = g_3^2/(4\pi)$ as $\alpha_s = 4\pi\,\alpha_3$, and similarly for α_w.

JHEP08(2017)004

Case	*Gauge couplings*		*Yukawa coupling*	*Type*	*Info*
	α_3^*	α_2^*	α_y^*		
FP$_1$	0	0	0	**G · G**	non-interacting
FP$_2$	0	$\frac{B_2}{C_2'}$	$\frac{F_2}{E}\,\alpha_2^*$	**G · GY**	partially interacting
FP$_3$	$\frac{B_3}{C_3'}$	0	$\frac{F_3}{E}\,\alpha_3^*$	**GY · G**	partially interacting
FP$_4$	$\frac{C_2'B_3 - B_2G_3'}{C_2'C_3' - G_2'G_3'}$	$\frac{C_3'B_2 - B_3G_2'}{C_2'C_3' - G_2'G_3'}$	$\frac{F_3}{E}\,\alpha_3^* + \frac{F_2}{E}\,\alpha_2^*$	**GY · GY**	fully interacting

Table 2. The four different types of UV fixed points FP$_1$–FP$_4$ in minimal BSM extensions of the SM with (3.7). The primed and unprimed loop coefficients are defined in appendix A. We also indicate how the fixed points can be interpreted as products of the Gaussian (G) and gauge-Yukawa (GY) fixed points when viewed from the individual gauge group factors (see main text).

A few comments are in order. The one loop gauge coefficients B_i can take either sign, depending on the BSM matter content. The two loop gauge coefficient C_2 is positive throughout. The two loop gauge coefficients C_3 may take either sign if $B_3 > 0$, but is strictly positive as soon as $B_3 \leq 0$ [11]. The two loop gauge mixing terms G_i as well as the two loop Yukawa contribution D_i and the one loop Yukawa terms E and F_i are always positive in any quantum field theory. The Yukawa couplings always contribute with a negative sign to the running of gauge couplings. This is centrally important for interacting UV fixed points to arise at weak coupling.

Explicit expressions for the various loop coefficients and further details are summarised in the appendix, see (A.2)–(A.6). In the absence of BSM matter fields, the RG flow (3.7) reduces to the RG flow of the SM with loop parameters given by (A.9). In this limit, the RG flow for the BSM Yukawa coupling becomes obsolete. With (3.7) at hand, we now turn to a systematic fixed point search within the perturbative regime.

3.3 UV fixed points at weak coupling

Gauge-Yukawa theories with (3.7) may display up to four different types of weakly coupled UV fixed points, depending on whether the gauge couplings take free or interacting values in the UV. We refer to the different cases as FP$_1$–FP$_4$, defined as

$$\begin{aligned} \text{FP}_1: &\quad \alpha_2^* = 0\,, &\quad \alpha_3^* = 0\,,\\ \text{FP}_2: &\quad \alpha_2^* > 0\,, &\quad \alpha_3^* = 0\,,\\ \text{FP}_3: &\quad \alpha_2^* = 0\,, &\quad \alpha_3^* > 0\,,\\ \text{FP}_4: &\quad \alpha_2^* > 0\,, &\quad \alpha_3^* > 0\,, \end{aligned} \tag{3.8}$$

see table 2 and 3. The Gaussian fixed point FP$_1$, where all couplings vanish, always exists. It qualifies as a candidate for an asymptotically free extension of the SM provided that each gauge sector remains asymptotically free individually. Using the explicit expressions (A.2)

JHEP08(2017)004

#	*Gauge couplings*		*BSM Yukawa*	*Type & info*	
FP$_1$	$\alpha_3^* = 0$	$\alpha_2^* = 0$	$\alpha_y^* = 0$	**G · G**	non-interacting
FP$_2$	$\alpha_3^* = 0$	$\alpha_2^* > 0$	$\alpha_y^* > 0$	**G · GY**	partially interacting
FP$_3$	$\alpha_3^* > 0$	$\alpha_2^* = 0$	$\alpha_y^* > 0$	**GY · G**	partially interacting
FP$_4$	$\alpha_3^* > 0$	$\alpha_2^* > 0$	$\alpha_y^* > 0$	**GY · GY**	fully interacting

Table 3. The four different types of UV fixed points FP$_1$–FP$_4$ in minimal BSM extensions of the SM with (3.7). The primed and unprimed loop coefficients are defined in appendix A. We also indicate how the fixed points can be interpreted as products of the Gaussian (G) and gauge-Yukawa (GY) fixed points when viewed from the individual gauge group factors (see main text).

FP$_3$				$\boldsymbol{R_2 = 1}$		$\boldsymbol{R_2 = 2}$		$\boldsymbol{R_2 = 3}$	
$\boldsymbol{R_3}$	(p,q)	$C_2(R_3)$	$S_2(R_3)$	$N_{\rm AF}$	$N_{\rm AS}$	$N_{\rm AF}$	$N_{\rm AS}$	$N_{\rm AF}$	$N_{\rm AS}$
3	(1,0)	$\frac{4}{3}$	$\frac{1}{2}$	10	–	6	–	3	–
6	(2,0)	$\frac{10}{3}$	$\frac{5}{2}$	2	(29) 37	1	(60) 77	–	(90) 117
8	(1,1)	3	3	1	(62) 96	–	(127) 198	–	(192) 299
10	(3,0)	6	$\frac{15}{2}$	–	(16) 18	–	(32) 34	–	(48) 51
15	(2,1)	$\frac{16}{3}$	10	–	(28) 30	–	(55) 60	–	(82) 90
15′	(4,0)	$\frac{28}{3}$	$\frac{35}{2}$	–	(16) 18	–	(32) 33	–	(48) 50

Table 4. Asymptotic freedom versus asymptotic safety at the partially interacting fixed point FP$_3$: shown are the maximal numbers of BSM fermion flavors compatible with asymptotic freedom, $N_{\rm AF}$, and the smallest number of flavors required for an asymptotically safe fixed point FP$_3$ to exist, $N_{\rm AS}$, both in dependence on the fermion representations R_2 and R_3 under SU(2)$_L$ and SU(3)$_C$, respectively. $N_{\rm AS}$ values in brackets relate to the absolute lower bound, those without to fixed points with $0 < \alpha_3^*, \alpha_y^* < 1$. Also indicated are the weights (p,q), quadratic Casimir, and Dynkin index under SU(3).

this condition translates into bounds

$$\begin{aligned} \mathrm{SU}(2)_L: &\quad N_F < 19/\big(8\, S_2(R_2)\, d(R_3)\big)\,, \\ \mathrm{SU}(3)_C: &\quad N_F < 21/\big(4\, S_2(R_3)\, d(R_2)\big)\,. \end{aligned} \tag{3.9}$$

In tables 4 and 5 we show the maximal number of BSM vector-like fermions $\psi(R_3, R_2)$ compatible with asymptotic freedom, $N_F \leq N_{\rm AF}$ for SU(2)$_L$ singlets, doublets and triplets, and for different dimensions of the SU(3)$_C$ representations. We observe a small window for low-dimensional representations where asymptotic freedom persists. Asymptotic freedom is lost as soon as the BSM fermions transform under higher-dimensional representations of the gauge group. See [5] for a recent analysis of BSM extensions with complete asymptotic freedom.

Theories with (3.7) may also display weakly interacting fixed points with $\alpha^* \leq 1$. These are either partially or fully interacting. Conditions for existence of partially interacting UV fixed points such as FP$_2$ and FP$_3$ then reduce to those given in section 2.1 for simple gauge theories. Analogous conditions of existence arise for the fully interacting fixed point FP$_4$. In either of theses cases, for FP$_2$, FP$_3$ or FP$_4$ to qualify as asymptotically safe UV fixed

JHEP08(2017)004

$\mathbf{FP_2}$				$\boldsymbol{R_3 = 1}$		$\boldsymbol{R_3 = 3}$		$\boldsymbol{R_3 = 6}$	
$\boldsymbol{R_2}$	ℓ	$C_2(R_2)$	$S_2(R_2)$	$N_{\rm AF}$	$N_{\rm AS}$	$N_{\rm AF}$	$N_{\rm AS}$	$N_{\rm AF}$	$N_{\rm AS}$
2	$\frac{1}{2}$	$\frac{3}{4}$	$\frac{1}{2}$	4	–	1	–	–	–
3	1	2	2	1	(26) 53	–	(73) 154	–	(145) 307
4	$\frac{3}{2}$	$\frac{15}{4}$	5	–	(7) 9	–	(21) 24	–	(41) 47
5	2	6	10	–	(6) 7	–	(17) 18	–	(33) 35
6	$\frac{5}{2}$	$\frac{35}{4}$	$\frac{35}{2}$	–	(6) 7	–	(16) 17	–	(31) 33

Table 5. Asymptotic freedom versus asymptotic safety at the partially interacting fixed point FP_2: shown are the maximal numbers of BSM fermion flavors $N_F < N_{\rm AF}$ compatible with asymptotic freedom, and the smallest number $N_F \geq N_{\rm AS}$ required for a weakly-coupled asymptotically safe fixed point, both in dependence on the fermion representations R_2 and R_3 under $\mathrm{SU}(2)_L$ and $\mathrm{SU}(3)_C$, respectively. Values for $N_{\rm AS}$ in brackets relate to the absolute lower bound, those without brackets to settings with $0 < \alpha_2^*, \alpha_y^* < 1$. Also indicated are the weight ℓ, the quadratic Casimir, and the Dynkin index under $\mathrm{SU}(2)_L$.

points, the Yukawa coupling must take an interacting fixed point by itself. To the leading non-trivial order in perturbation theory, using (3.7), it follows that the Yukawa coupling at a fixed point is linearly related to the gauge couplings,

$$\begin{aligned} \mathrm{FP}_2: &\qquad \alpha_y^* = \frac{F_2}{E}\,\alpha_2^*\,, \\ \mathrm{FP}_3: &\qquad \alpha_y^* = \frac{F_3}{E}\,\alpha_3^*\,, \\ \mathrm{FP}_4: &\qquad \alpha_y^* = \frac{F_2}{E}\,\alpha_2^* + \frac{F_3}{E}\,\alpha_3^*\,, \end{aligned} \tag{3.10}$$

depending on whether α_2, or α_3, or both, take interacting fixed points by themselves. Combining (3.10) with the vanishing of the gauge beta functions provides explicit expressions for the different fixed points. An overview of fixed points and their properties is given in table 2 and 3. Next we analyse minimal conditions that need to be fulfilled in the BSM sector in order to generate partially or fully interacting UV fixed points in the system (3.7).

3.4 Partially interacting fixed points

The partially interacting fixed points FP_2 and FP_3 are characterised by one of the gauge couplings, say $\alpha_{\rm AS}$, taking an asymptotically safe fixed point in the UV whereby the other gauge coupling, say $\alpha_{\rm AF}$, becomes asymptotically free. The Yukawa couplings must take interacting values, $\alpha_y^* \propto \alpha_{\rm AS}^*$, see (3.10). The beta functions (3.7) then take the simplified form

$$\begin{aligned} \beta_{\rm AS} &= (-B_{\rm AS} + C_{\rm AS}\,\alpha_{\rm AS} - D_{\rm AS}\,\alpha_y)\,\alpha_{\rm AS}^2\,, \\ \beta_y &= (E\,\alpha_y - F_{\rm AS}\,\alpha_{\rm AS})\,\alpha_y\,. \end{aligned} \tag{3.11}$$

These expressions formally agree with (2.1) and therefore offer the same type of fixed point solutions. The non-trivial UV fixed point is then of the form (2.5), (2.6), after substituting the appropriate loop coefficients. A minimal requirement for partially interacting fixed

JHEP08(2017)004

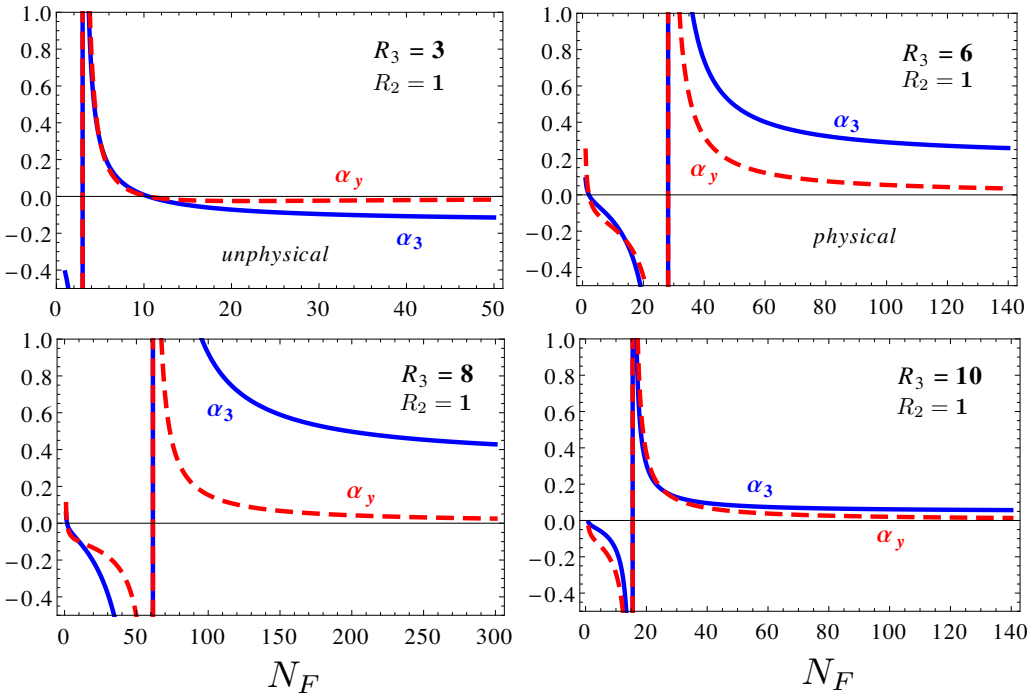

Figure 1. Partially interacting fixed point FP_3 with $\alpha_2^* = 0$, showing the strong coupling α_3^* (blue, solid line) and the BSM Yukawa coupling α_y^* (red, dashed) versus the number N_F of the BSM flavors for $R_2 = \mathbf{1}$ and different $\mathrm{SU}(3)_C$ representations $R_3 = \mathbf{3}, \mathbf{6}, \mathbf{8}$ and $\mathbf{10}$ (see main text).

points to be UV fixed points is the loss of asymptotic freedom in the gauge sector $B_{\mathrm{AS}} < 0$, meaning either

$$\begin{aligned} &\mathrm{FP}_2: \quad N_F > 19/\big(8\, S_2(R_2)\, d(R_3)\big)\,, \\ \text{or}\quad &\mathrm{FP}_3: \quad N_F > 21/\big(4\, S_2(R_3)\, d(R_2)\big)\,, \end{aligned} \tag{3.12}$$

thus reverting the condition (3.9). Associating suitable charges to the BSM fermions, it is then possible to satisfy either of the conditions in (3.12). Furthermore, the physicality condition (2.7) translates into

$$\begin{aligned} &\mathrm{FP}_2: \quad D_2\, F_2 - E\, C_2 > 0\,, \\ &\mathrm{FP}_3: \quad D_3\, F_3 - E\, C_3 > 0\,. \end{aligned} \tag{3.13}$$

It remains to evaluate solutions to the conditions (3.13) separately for FP_2 and FP_3, to which we turn next.

Strong strong and weak weak gauge coupling. In figure 1 we analyse the condition (3.13) exemplarily for FP_3 where the strong coupling remains interacting in the deep UV whereas the weak coupling vanishes asymptotically. We assume that the BSM fermions carry no $\mathrm{SU}(2)_L$ charges ($R_2 = \mathbf{1}$), but different $\mathrm{SU}(3)_C$ representations $R_3 = \mathbf{3}, \mathbf{6}, \mathbf{8}$ and $\mathbf{10}$. We observe the following pattern. For fermions in the fundamental, a narrow window of weakly interacting fixed points exists for a low number of flavors N_F. These low-N_F solutions come out as IR fixed points in that they relate to settings with asymptotic freedom

JHEP08(2017)004

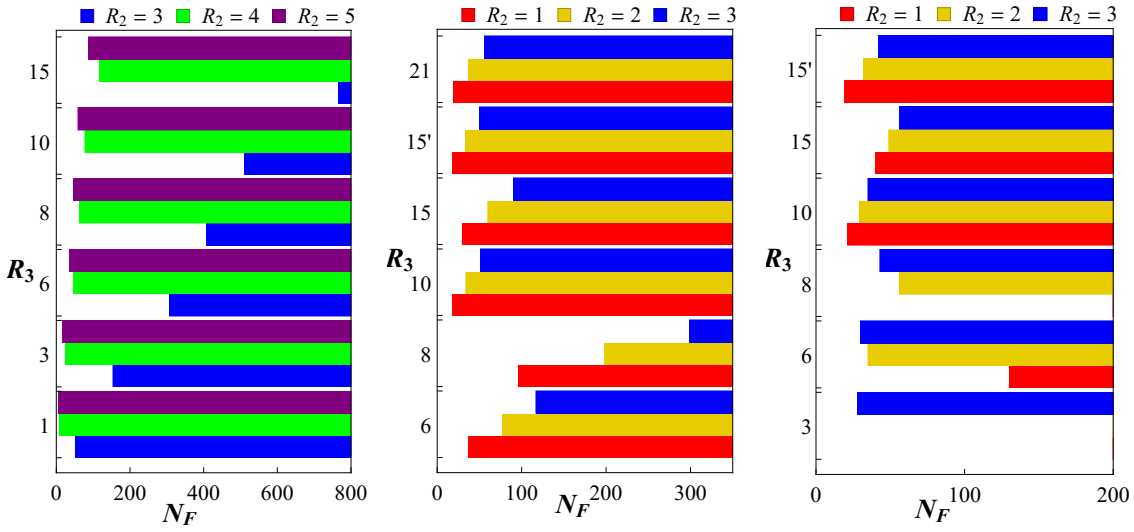

Figure 2. Availability of weakly interacting UV fixed points FP_2 (left panel), FP_3 (middle panel), and FP_4 (right panel) in dependence on the representation (R_2, R_3) and the flavor multiplicities N_F of BSM fermions. The pattern of results continues to higher (R_2, R_3). Partially interacting fixed points FP_2 are absent for any N_F as soon as $R_2 = \mathbf{1}$ or $\mathbf{2}$; FP_3 is absent whenever $R_3 = \mathbf{1}$ or $\mathbf{3}$; fully interacting UV fixed points FP_4 are absent for $R_3 = \mathbf{1}$ or $(R_2, R_3) = (\mathbf{1}, \mathbf{8}), (\mathbf{2}, \mathbf{3})$, and $(\mathbf{1}, \mathbf{3})$.

in both gauge sectors (see the discussion in section 3.8). With increasing N_F, the fixed point takes negative values and becomes unphysical. Conversely, for fermions in higher-dimensional representations (anything but the fundamental), we find that a fixed point exists for sufficiently large N_F. No fixed points exist for intermediate values of N_F. Occasionally we find that fixed points can exist for exceptionally low values of N_F, in which case the fixed point is IR rather than UV. In figure 2 (middle panel), we show the set of parameters (R_2, R_3, N_F) for which FP_3 exists as an interacting UV fixed point. In table 4 we summarise the minimum number of BSM fermions N_{AS} which lead to a weakly coupled UV fixed point with $\alpha^* \leq 1$.

The pattern of results is easily understood once N_F is sufficiently large. The necessary condition for existence (3.13) of FP_3 turns into a quadratic polynomial in N_F after inserting the explicit expressions for the loop coefficients,

$$X\, N_F^2 + Y\, N_F - Z < 0\,, \tag{3.14}$$

with coefficients

$$\begin{aligned} X &= Z\, C_2(R_3)\, [5 - 2C_2(R_3)]/52\,, \\ Y &= Z^2[C_2(R_3) + 5]/52 - C_2(R_3)\,, \\ Z &= C_2(R_3) d(R_3) d(R_2)\,, \end{aligned} \tag{3.15}$$

and with $C_2(R)$ and $d(R)$ defined in (A.8). For sufficiently large N_F, the sign of the coefficient X dictates whether the condition (3.14) provides an upper or a lower bound on N_F. If $X > 0$, the condition (3.14) provides an upper bound on the number of the BSM

JHEP08(2017)004

fermions. However, we observe that $X > 0$ if and only if the BSM fermions transform under the fundamental representation of $\mathrm{SU}(3)_C$ (see table 4 for explicit values of the Casimir invariant for several R_3 of the lowest dimension). In this case it is readily confirmed that a solution to (3.14) is incompatible with the lower bound from (3.9) for any choice of R_3, meaning that such a fixed point is necessarily an IR fixed point. We conclude that asymptotic safety via a partially interacting fixed point cannot be achieved within the fundamental representation of $\mathrm{SU}(3)_C$. On the other hand, for higher-dimensional representations the coefficient X becomes negative. Consequently, (3.14) provides a lower bound on the number of BSM fermions required to achieve asymptotic safety, $N_F \geq N_{\mathrm{AS}}$. The case $X = 0$ has no physical solutions. Exemplary values for the lower bound , $N_F \geq N_{\mathrm{AS}}$ for different representations R_3 and R_2 are given in table 4, where we additionally require weak coupling $\alpha_i^* < 1$ at the fixed point.

Strong weak and weak strong gauge coupling. Next we turn to FP_2 where the weak sector remains interacting in the deep UV whereas the strong coupling becomes asymptotically weak. Qualitatively, our findings for FP_2 are very similar to those discussed previously for FP_3. The absence of asymptotic freedom in the $\mathrm{SU}(2)_L$ gauge sector, (3.12), requires a minimal number of BSM fermion flavors $N_F \geq N_{\mathrm{AF}}$. In figure 2 (left panel), we show the set of parameters (R_2, R_3, N_F) for which FP_2 exists as an interacting UV fixed point. In table 5, we provide N_{AF} for $\mathrm{SU}(3)_C$ singlets, triplets and sextets, and for different dimensions of the $\mathrm{SU}(2)_L$ representations. Since the SM contribution to the one-loop gauge coefficient is larger for $\mathrm{SU}(2)_L$ than for $\mathrm{SU}(3)_C$, lower values for N_F and lower dimensions of representations are required to lose asymptotic freedom for $\mathrm{SU}(2)_L$. Similarly, from (3.13) we find that asymptotic safety cannot be achieved with fermions in the fundamental representations of $\mathrm{SU}(2)_L$. The minimal number of BSM fermion flavors required for a weakly-coupled asymptotically safe fixed point, N_{AS}, are given in table 5 for various choices of R_2 and R_3.

3.5 Regaining asymptotic freedom

Next we discuss the fate of the gauge coupling which vanishes at partially interacting fixed points FP_2 or FP_3, and which we denote for notational simplicity as α_{AF}. The coupling α_{AF} must be asymptotically free for a partially interacting fixed point to be viable, or else the UV fixed point cannot be reached by any finite RG trajectory along the α_{AF} direction. In general, we find that B_{AF} becomes negative as soon as BSM fermions carry charges of both gauge groups. However, the sign of B_{AF} plays no role, as it no longer dictates whether this sector remains asymptotically free or not. Rather, to leading order in the asymptotically free gauge coupling, we have

$$\beta_{\mathrm{AF}} = (-B_{\mathrm{AF}} + G_{\mathrm{AF}}\,\alpha_{\mathrm{AS}}^* - D_{\mathrm{AF}}\,\alpha_y^*)\,\alpha_{\mathrm{AF}}^2 + \mathcal{O}(\alpha_{\mathrm{AF}}^3)\,, \tag{3.16}$$

showing that the one loop coefficient B_{AF} is replaced by $B'_{\mathrm{AF}} = B_{\mathrm{AF}} - G_{\mathrm{AF}}\,\alpha_{\mathrm{AS}}^* + D_{\mathrm{AF}}\,\alpha_y^*$. We stress that this shift is a consequence of partially interacting fixed points. It arises from residual interactions at the UV fixed point due to asymptotic safety of the gauge coupling α_{AS} and the BSM Yukawa coupling. Their residual interactions modify the running of

JHEP08(2017)004

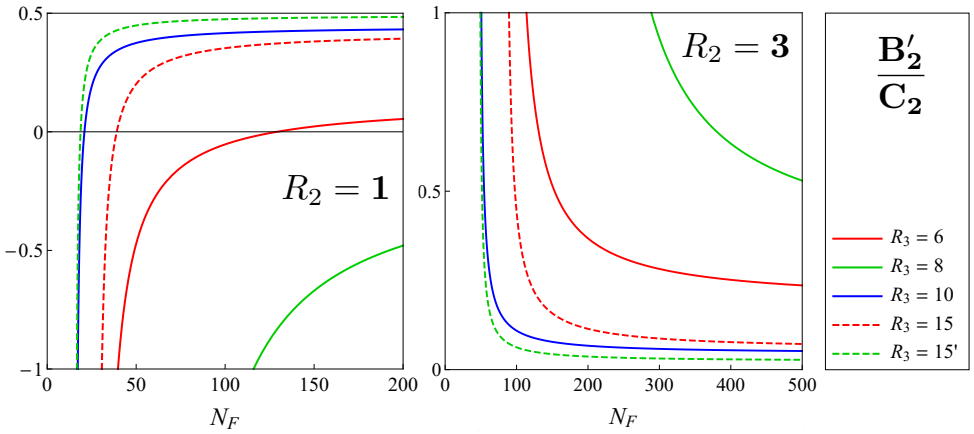

Figure 3. Asymptotic freedom at partially interacting fixed points FP_3. Shown is the condition for asymptotic freedom (3.17) for the effective coefficient B_2' in units of the two loop coefficient $C_2 > 0$ at FP_3 for, exemplarily, $R_2 = \mathbf{1}$ (left panel) and $R_2 = \mathbf{3}$ (right panel), and as a function of R_3 (color coding given in the legend). We observe that asymptotic freedom in the weak sector is regained as soon as $R_2 > \mathbf{1}$ and $R_3 > \mathbf{3}$, for any N_F. For $R_2 = \mathbf{1}$, a lower bound on N_F is found (left panel). Qualitatively and quantitatively similar results are obtained at FP_2 (not displayed).

the asymptotically free coupling owing to fermions which carry charges under both gauge groups. Provided that the shifted one loop coefficients B' take positive values,

$$B'_{\mathrm{AF}} > 0\,, \tag{3.17}$$

the non-interacting gauge sector becomes asymptotically free in the deep UV. We also stress that the BSM Yukawa interactions play a central role: only Yukawa couplings add negatively to the beta function (3.16). Without them, (3.17) cannot be achieved starting from $B_{\mathrm{AF}} < 0$. Using (3.7), we have the following expressions for the shifted one loop coefficients

$$\begin{aligned} \mathrm{FP}_2: &\qquad B_3 \to B_3' = B_3 - G_3\,\alpha_2^* + D_3\,\alpha_y^*\,, \\ \mathrm{FP}_3: &\qquad B_2 \to B_2' = B_2 - G_2\,\alpha_3^* + D_2\,\alpha_y^*\,. \end{aligned} \tag{3.18}$$

We conclude that (3.17), (3.18) are necessary conditions for the corresponding partially interacting fixed point to qualify as UV completions of the SM.

In figure 3 the condition for asymptotic freedom (3.18) at FP_3 is shown for models with $R_2 = \mathbf{1}$ (left panel) and $R_2 = \mathbf{3}$ (right panel) and various $R_3 > \mathbf{3}$ (recall that there are no viable UV fixed points FP_3 for $R_3 \leq \mathbf{3}$, figure 2). If $R_2 = \mathbf{1}$, we observe that B_2' is positive for sufficiently large N_F, and negative for sufficiently low N_F, thus leading to a lower bound. Conversely, if $R_2 = \mathbf{3}$ (or larger), the sign of B_2' is always positive. In this case asymptotic freedom is guaranteed without any further constraints as soon as α_3 is asymptotically safe. The same pattern of results holds true for FP_2. We conclude that as soon as the BSM fermions carry a non-trivial charge under the asymptotically free coupling $R_{\mathrm{AF}} \neq \mathbf{1}$, for any $R_{\mathrm{AS}} \neq \mathbf{1}$, the condition (3.17) follows from the condition for asymptotic safety for α_{AS} (3.13). For BSM fermions with $R_{\mathrm{AF}} = \mathbf{1}$, (3.17) entails an additional lower bound on N_F.

JHEP08(2017)004

FP$_4$	$R_3 = 1$	$R_3 = 3$	$R_3 = 6$	$R_3 = 8$	$R_3 = 10$
R_2	$N_{\rm AS}$	$N_{\rm AS}$	$N_{\rm AS}$	$N_{\rm AS}$	$N_{\rm AS}$
1	–	–	(130) 130	–	(21) 21
2	–	–	(29) 35	(45) 56	(27) 29
3	–	(23) 28	(27) 30	(38) 43	(33) 35
4	–	(17) 18	(26) 28	(36) 39	(37) 39
5	–	(15) 16	(27) 28	(36) 38	(40) 42

Table 6. The minimal number of the BSM fermions flavors $N_F \geq N_{\rm AS}$ required for the fully interacting fixed point FP$_4$ to exist, in dependence on the fermion representations R_2 and R_3 under SU(2)$_L$ and SU(3)$_C$. The values for $N_{\rm AS}$ in brackets relate to the absolute lower bound, and those without to settings with $0 < \alpha_3^*, \alpha_2^*, \alpha_y^* < 1$.

3.6 Fully interacting fixed points

Finally we consider the case FP$_4$. In the case where both gauge couplings and the BSM Yukawa coupling remain weakly interacting at the fixed point in the asymptotic UV the overall behaviour of the system (3.7) depends on the interplay between one- and two-loop coefficients. Using the results of table 2, the necessary condition for a fixed point can be stated as

$$\alpha_2^* = \frac{C_3' B_2 - B_3 G_2'}{C_2' C_3' - G_2' G_3'} > 0\,, \qquad \alpha_3^* = \frac{C_2' B_3 - B_2 G_3'}{C_2' C_3' - G_2' G_3'} > 0\,, \tag{3.19}$$

with primed two-loop coefficient given in (A.11). Unlike the condition for partially interacting fixed points (3.13), those for fully interacting ones involve ratios of differences of Yukawa-shifted loop coefficients. In particular, fully interacting fixed points may exist even if only one of the conditions (3.13) is satisfied. For the purpose of this work, we have investigated the conditions (3.19) numerically. In figure 2 (right panel), we show the set of parameters (R_2, R_3, N_F) for which FP$_4$ exists as an interacting UV fixed point. Our results for the lowest number of flavor multiplicities $N_F \geq N_{\rm AS}$ are summarised in table 6.

3.7 Large-N_F approximation

Some analytical insights about interacting UV fixed points can be obtained in the limit of many flavors of fermions $N_F \gg 1$, which we discuss separately for either type of fixed point.

Partially interacting fixed points. For a partially interacting fixed point, and using the explicit solution for FP$_3$ as given in table 3, the large-N_F approximation leads to

$$(\alpha_3^*, \alpha_2^*, \alpha_y^*)\big|_{N_F \gg 1} = \frac{1}{X_3}\left(\frac{1}{3}\,, 0\,, \frac{2C_2(R_3)}{N_F}\right) + \text{subleading}\,, \tag{3.20}$$

where $X_3(R_3) = 2C_2(R_3) - 5$. The subleading terms are at least one power in N_F smaller than the leading order terms. Several observations can now be made. First of all, positivity of the fixed point couplings requires $X_3(R_3) > 0$ or $C_2(R_3) > \frac{5}{2}$. Hence, our result confirms that asymptotic safety cannot be achieved within the fundamental representations of

JHEP08(2017)004

$\mathrm{SU}(3)_C$ even at large-N_F, owing to $X_3(\text{fund.}) < 0$. Secondly, we observe that the Yukawa coupling scales like $1/N_F$ and can always be made arbitrarily small. Conversely, the size of the gauge coupling is solely determined by the quadratic Casimir $C_2(R_3)$, and independent of N_F in the large-N_F limit. We stress that (3.20) is parametrically close to the Gaussian fixed point, provided that X_3 becomes parametrically large. In addition, the necessary condition for asymptotic freedom (3.17) for the weak coupling simplifies to leading order at large-N_F and reads $C_2(R_3) > \frac{5}{2}$. Interestingly, the condition for asymptotic freedom exactly coincides with the condition for asymptotic safety of (3.20) at large-N_F,

$$C_2(R_3) > \frac{5}{2}\,, \quad \text{or} \quad R_3 \geq \mathbf{6}\,. \tag{3.21}$$

We conclude that higher dimensional representations under $\mathrm{SU}(3)_C$ with (3.20) are favoured for the theory to display a perturbative UV fixed point in the $\mathrm{SU}(3)_C$ coupling, and for $\mathrm{SU}(2)_L$ sector to regain asymptotic freedom at the partially interacting UV fixed point FP_3, see figure 1. Analogous results are established for FP_2, where the large-N_F expansion starts off with

$$(\alpha_3^*, \alpha_2^*, \alpha_y^*)\big|_{N_F \gg 1} = \frac{1}{X_2}\left(0\,, \frac{1}{2}\,, \frac{3C_2(R_2)}{N_F}\right) + \text{subleading}\,, \tag{3.22}$$

and $X_2(R_2) = 3C_2(R_2) - 5$. Again, subleading terms are suppressed by at least one additional power in N_F over the leading terms. A necessary condition for asymptotic safety is $X_2(R_2) > 0$, thus excluding the fundamental representation owing to $X_2(\text{fund.}) < 0$. We also conclude that FP_2 is parametrically close to the Gaussian fixed point in the limit of high-dimensional representations X_2. Furthermore, to leading order at large-N_F the condition for asymptotic freedom (3.17) for the strong coupling becomes

$$C_2(R_2) > \frac{5}{3}\,, \quad \text{or} \quad R_2 \geq \mathbf{3}\,. \tag{3.23}$$

Once more, this secondary condition coincides with the condition for asymptotic safety of (3.22).

Fully interacting fixed points. For the fully interacting fixed point, using the explicit solution for FP_4 as given in table 2 and performing a large-N_F limit, we find

$$(\alpha_3^*, \alpha_2^*, \alpha_y^*)\big|_{N_F \gg 1} = \frac{1}{X_{32}}\left(\frac{1}{3}\,, \frac{1}{2}\,, \frac{2C_2(R_3) + 3C_2(R_2)}{N_F}\right) + \text{subleading}\,, \tag{3.24}$$

with $X_{32} = 2C_2(R_3) + 3C_2(R_2) - 5$. The above expression holds true provided that $R_3 \neq \mathbf{1}$ and $R_2 \neq \mathbf{1}$. The requirement of asymptotic safety results in an inequality $X_{32} > 0$. Furthermore, the result also shows that the fully interacting fixed point is parametrically close to the Gaussian provided that X_{32} is large. The explicit result explains why a fully interacting fixed point with asymptotic safety can be achieved even with BSM fermions in the fundamental representation of $\mathrm{SU}(3)_C$, as long as they transform under $\mathrm{SU}(2)_L$ in a representation of a dimension higher than the fundamental. Analogously, FP_4 exists for BSM fermions in the fundamental representation of $\mathrm{SU}(2)_L$ provided that $R_3 > \mathbf{3}$. Note

JHEP08(2017)004

that these large-N_F estimates are in very good agreement with the numerical findings in table 6. In the special case where $R_3 > \mathbf{1}$ and $R_2 = \mathbf{1}$, and instead of (3.24), one obtains

$$(\alpha_3^*, \alpha_2^*, \alpha_y^*)\big|_{N_F \gg 1} = \left(\frac{1}{3X_{32}}\,,\ \frac{19}{35} - \frac{24}{35X_{32}}\,,\ \frac{2C_2(R_3)}{N_F X_{32}} \right) + \text{subleading}\,, \tag{3.25}$$

with $X_{32} = 2C_2(R_3) + 3C_2(R_2) - 5$ as before. Notice that this fixed point is parametrically close to the "would-be" Banks-Zaks fixed point in the $\mathrm{SU}(2)_L$ sector of the SM. The condition for existence is now given by $X_{32} > \frac{24}{19}$ which translates into $C_2(R_3) > 3\frac{5}{38}$. Solutions are given by the $R_3 = \mathbf{6}$ and $R_3 \geq \mathbf{10}$ representations under $\mathrm{SU}(3)_C$. Curiously, the adjoint representation $R_3 = \mathbf{8}$ with $R_2 = \mathbf{1}$ is not a solution of (3.25) owing to the "would-be" Banks-Zaks IR fixed point. Finally, for $R_3 = \mathbf{1}$ and $R_2 \geq \mathbf{1}$ one readily confirms that α_3^* and α_2^* cannot simultaneously take positive values meaning that an asymptotically safe fixed point does not arise at large N_F.

3.8 Synopsis of UV fixed points

We are now in a position to summarise the main results for weakly interacting UV fixed points in extensions of the SM of the form (3.3). We have observed that interacting UV fixed points can arise as partially or fully interacting ones. In either of these cases, necessary conditions for their existence have been found, providing us with constraints on the remaining BSM parameters (R_3, R_2, N_F). We have also observed that for fixed (R_3, R_2), UV fixed points typically exists for all N_F down to limiting values specified in table 4, 5 and 6. Figure 4 shows a summary of our findings, in dependence on the fermion representation (R_3, R_2) under $\mathrm{SU}(3)_C \otimes \mathrm{SU}(2)_L$ with different symbols relating to the different fixed points FP_2, FP_3, and FP_4. Broadly speaking, results show the existence of fixed points both with increasing dimensionality of the fermion representation, and with increasing flavor multiplicities. Similarly, fixed points come out less strongly coupled the larger their dimensionality R_2, R_3 and the flavor multiplicity N_F. We also observe that different types of fixed points might coexist for BSM fermions with the same set of representations (R_2, R_3), starting from a lowest value for N_F where the fixed point arises for the first time. In figure 4 the possibility of coexistence is indicated by overlapping symbols: the lower lying symbol relates to a fixed point which arises for larger N_F.

Hence, four distinct cases arise: (i) for high dimensional representations, starting from $R_2 = \mathbf{3}$ and $R_3 = \mathbf{6}$ onward, all three types of fixed points are realised starting from some lowest value for N_F. For fixed (R_2, R_3) but with increasing N_F results show that the fully interacting fixed point FP_4 is achieved first, followed by the partially interacting FP_3 for the strong coupling, and ultimately followed by the partially interacting fixed point FP_2 in the weak coupling. (ii) If the fermions are in the fundamental representation of one of the two gauge groups, we find that the corresponding partially interacting fixed point is absent throughout. However, the other two fixed points still exist and the order in which they appear, with increasing N_F, is exactly the same as the order observed for the higher dimensional representations. (iii) If the BSM fermions are uncharged under $\mathrm{SU}(3)_C$, only the partially interacting fixed point FP_2 can arise, starting from $R_2 = \mathbf{3}$ onwards. (iv) If the BSM fermions are uncharged under $\mathrm{SU}(2)_L$, we find that FP_3 arises first, followed by

JHEP08(2017)004

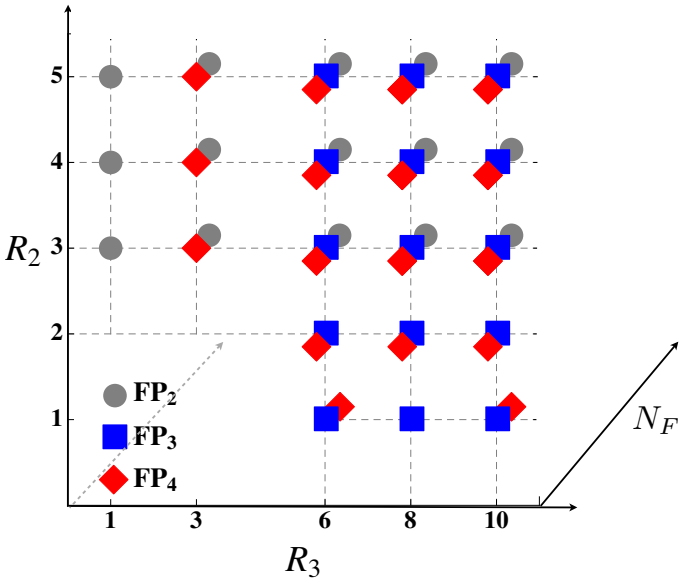

Figure 4. Summary of weakly interacting UV fixed points of (3.7) in dependence on the fermion representation and flavor multiplicities (R_3, R_2, N_F). The different symbols relate to FP_2 (gray circle), FP_3 (blue square) and FP_4 (red diamond). Overlapping symbols indicate that either type of fixed point can exist, with lower-lying symbols relating to fixed points which arise at a higher number of fermion flavors N_F, see also figure 2.

FP_4, while FP_2 is absent throughout. This holds true for all $R_3 = \mathbf{6}$ or higher, except for $R_3 = \mathbf{8}$ where only FP_3 appears.

Finally, we discuss the status of interacting fixed points for low numbers of flavors N_F. The low-N_F partially interacting fixed points FP_3 at $R_2 = \mathbf{1}$ with $R_3 = \mathbf{3}, \mathbf{6}$ and $\mathbf{8}$ all have $B_2, B_3 > 0$, (3.9). Hence the theory remains asymptotically free in both gauge group factors, and the interacting fixed point is formally an IR fixed point of the type discussed in table 1 **b)**. Similarly, for FP_2 and FP_4 we find a handful of low-N_F fixed points all of which occur where asymptotic freedom persists in both gauge groups (3.9). Conversely, we also have low-N_F fixed points FP_3 with $R_2 = \mathbf{2}, \cdots, \mathbf{10}$ which have asymptotic freedom only in the strong gauge coupling, while the weak sector has become infrared free. Such fixed points are not of phenomenological interest because they cannot be linked with any finite $\alpha_2 \neq 0$ in the IR and shall be dropped.

This completes our investigation of weakly coupled UV fixed points of (3.3) to the leading non-trivial order in perturbation theory, (3.7). In the next section, we explain whether and how these fixed points are connected with the SM at low energies under the RG evolution of couplings.

4 Matching onto the Standard Model

In this section, we evaluate the conditions under which BSM trajectories emanating out of interacting UV fixed points are connected with the SM at low energies.

JHEP08(2017)004

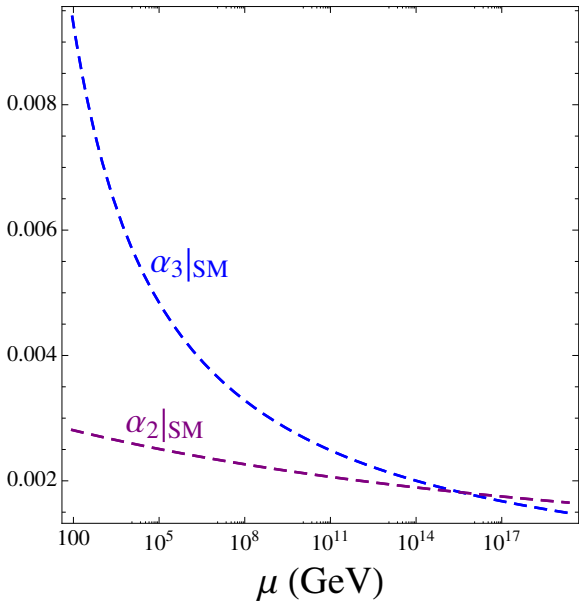

Figure 5. SM running of the strong and weak gauge coupling α_3 (blue) and α_2 (purple) from the Z mass up to Planckian energies. The SM GUT scale reads approximately $\mu_{\rm GUT} \approx 4 \times 10^{15}\,$GeV. UV safe trajectories have to coincide with SM values at the matching scale $\mu = M$ where BSM matter decouples.

4.1 Matching conditions

Any RG trajectory emanating from free or interacting UV fixed points qualifies as a UV complete quantum field theory. The UV critical surface then determine the set of UV-safe trajectories. The relevant or marginally relevant couplings in the UV determines the dimensionality of the UV critical surface (2.9). Conversely, the irrelevant couplings are uniquely fixed by the relevant couplings in the UV. Consequently, the number of fundamentally free parameters which characterise the UV-safe trajectories is given by the dimensionality of the UV critical surface. At low energies, physically viable BSM trajectories must connect with those of the SM, see figure 5, as soon as the BSM matter fields have decoupled.

It remains to check whether the UV fixed points discovered in the previous section are connected through well-defined RG trajectories to the SM at low energies. Away from the fixed point, BSM matter fields will develop scalar and fermion masses M_S and M_ψ which are independent parameters of the theory. Phenomenological constraints for M_S and M_ψ are worked out in section 5 below. For RG scales much larger than the masses, the BSM matter fields are effectively massless, and the RG flow is given by (3.7). Conversely, for RG scales much lower than the masses, the BSM fields are taken to be infinitely heavy and decouple. The RG flow (3.7) reduces to the one of the SM, also restoring confinement of QCD at low energies. Hence, the BSM contributions to the running gauge couplings decouple as soon as μ is of the order of the BSM fermion mass. Furthermore, threshold effects are subleading to the overall picture and will be neglected. Consequently, the RG

JHEP08(2017)004

flow of the SM is matched onto the RG flow of the BSM extension at the matching scale M,

$$\mu = M \approx M_\psi \tag{4.1}$$

below which the BSM fermions decouple. This leads to matching conditions between the RG flow of the SM at scales below (4.1), and BSM flows (3.7) above the mass scale (4.1),

$$\alpha_i(\mu = M)\big|_{\rm SM} = \alpha_i(\mu = M)\big|_{\rm BSM}\,, \tag{4.2}$$

for $i = 2, 3$ (or $i = $AF,AS in settings with partially interacting fixed points). There will be no matching condition for the BSM Yukawa coupling since it is not part of the SM. Rather, after the decoupling of the BSM fields, the Yukawa coupling will "freeze out" at its value at decoupling. For the quantitative studies below, we use PDG SM reference values at the scale of the Z pole mass [22],

$$\begin{aligned} \alpha_2(\mu = m_Z) &= 2.7 \times 10^{-3}, \\ \alpha_3(\mu = m_Z) &= 9.5 \times 10^{-3}, \end{aligned} \tag{4.3}$$

together with the two loop perturbative running of gauge couplings in the SM, using (3.7) with $N_F = 0$. Figure 5 illustrates the SM running between the mass of the Z boson ($m_Z = 91.19\,\text{GeV}$) and Planckian energies. Note that equality of gauge couplings

$$\alpha_2(\mu) = \alpha_3(\mu) \tag{4.4}$$

arises in the SM at the GUT scale $\mu_{\rm GUT} \approx 4 \times 10^{15}\,\text{GeV}$. We emphasize that the matching of the BSM extension (3.7) onto the SM (4.2) takes place at perturbatively small couplings.

4.2 Partially interacting fixed points

As has been detailed in section 3.4, at partially interacting fixed points FP_2 and FP_3, one of the two gauge couplings becomes asymptotically free, while the other one becomes asymptotically safe. Moreover, the asymptotically (free) safe coupling is (marginally) relevant and, hence, the UV critical surface is invariably two-dimensional. On the other hand, the BSM Yukawa coupling α_y is irrelevant and fully specified by the asymptotically safe coupling in the UV.

In this light, a convenient choice for the two fundamentally free dimensionless parameters which characterise UV-safe trajectories running out of the fixed point are the deviations of the gauge couplings from their UV fixed point values at some high scale $\mu = \Lambda$,

$$\delta\alpha_i(\Lambda) = \alpha_i^* - \alpha_i(\Lambda)\,, \tag{4.5}$$

with $i = 2, 3$ (or $i = $AF,AS). We take the practical view that the high scale is essentially given by the Planck scale. Quantum gravity effects should be retained at scales close to and above Λ. The BSM Yukawa coupling is an irrelevant coupling and entirely dictated by the UV hypercritical surface relating it with $\alpha_{\rm AS}$ and $\alpha_{\rm AF}$,

$$\alpha_y = F_y(\alpha_{\rm AS}, \alpha_{\rm AF})\,. \tag{4.6}$$

JHEP08(2017)004

The parameters (4.5) will be used to match trajectories onto the SM. Specifically, the parameter $\delta\alpha_{\rm AS}$ controls at which energy scale the asymptotically safe coupling is crossing over from the UV fixed point towards the Gaussian IR fixed point of (3.7). For $0 < \delta\alpha_{\rm AS} \ll 1$, $\alpha_{\rm AS}$ will start out of the UV fixed point along the separatrix which connects the UV fixed point with the Gaussian in the IR. In the immediate vicinity of the UV fixed point the RG flow is of the power-law type and thus fast, controlled by the relevant scaling exponent. Further away from the fixed point, as soon as $\alpha_{\rm AS} \approx \frac{2}{3}\alpha^*_{\rm AS}$ and below [13], we observe a cross-over whereby the running becomes logarithmically slow instead, dominated by the "would-be" Gaussian IR fixed point of (3.7). Hence, the parameter $\delta\alpha_{\rm AS}$ allows us to chose at which scale $\alpha_{\rm AS}(M)$ has reached the desired SM value. Notice that this discussion is largely independent of $\alpha_{\rm AF}$ provided the latter remains small.

The running of $\alpha_{\rm AF}$ out of the UV fixed point is controlled by the RG flow (3.16), which in turn is largely determined by the parameter $\delta\alpha_{\rm AF}$, together with the coefficients $B_{\rm AF}$ and $B'_{\rm AF}$, (3.18). Integrating (3.16) close to the UV fixed point gives

$$\frac{1}{\alpha_{\rm AF}(\mu)} = \frac{1}{\delta\alpha_{\rm AF}(\Lambda)} + B'_{\rm AF}\ln(\mu/\Lambda)\,. \tag{4.7}$$

One might expect that the two free parameters (4.5) are sufficient to match the RG flow in the UV to two preset values at low energies. We stress, however, that a matching may fail if the "would-be" asymptotically free coupling $\alpha_{\rm AF}$ runs into Landau poles at intermediate energies. Thus, we must explain how Landau poles are avoided. In the deep UV, we have that $B'_{\rm AF} > 0$, (3.17). However, the coefficient $B'_{\rm AF}$ depends on the asymptotically safe gauge coupling $\alpha_{\rm AS}$ and on the Yukawa coupling. Both of these run out of the UV fixed point and induce an effective running of $B'_{\rm AF} \to B'_{\rm AF}(\mu)$ owing to (3.16). For sufficiently small $\alpha_{\rm AS}$ such as close to the matching scale $\mu = M$, the coefficient $B'_{\rm AF}$ falls back onto the BSM one loop coefficient $B'_{\rm AF} \to B_{\rm AF}$. Close to the matching scale the one loop approximation is viable and we have

$$\frac{1}{\alpha_i(\mu)} = \frac{1}{\alpha_i(M)} + B_i\ln(\mu/M) \tag{4.8}$$

for both $i = {\rm AF}, {\rm AS}$. If $B_{\rm AF} > 0$, meaning that the gauge sector remains asymptotically free, we have that $B'_{\rm AF}(\mu) > 0$ at all intermediate scales and matching will always be possible. If $B_i < 0$, the one loop running (4.8) for the gauge couplings reach a "would-be" Landau pole at

$$\frac{\mu_i}{M} = \exp\left(-\frac{1}{B_i\,\alpha_i(M)}\right). \tag{4.9}$$

For $\alpha_{\rm AS}$ the Landau pole is avoided automatically owing to the two loop Yukawa terms: with growing energy, once the scale $\mu_{\rm AS}$ is reached, the two loop terms kick in and $\alpha_{\rm AS}$ settles into its UV fixed point, see section 2. For $\alpha_{\rm AF}$ it is not guaranteed that $B'_{\rm AF}(\mu)$ changes sign in time for $\alpha_{\rm AF}$ to avoid the Landau pole. We find that $\alpha_{\rm AF}$ avoids a Landau pole provided that

$$B_{\rm AF}\cdot\alpha_{\rm AF}(M) < B_{\rm AS}\cdot\alpha_{\rm AS}(M)\,. \tag{4.10}$$

The condition (4.10) ensures that the "would-be" one loop Landau pole for $\alpha_{\rm AF}$ arises at higher scales $\mu_{\rm AF} > \mu_{\rm AS} > M$ than the one for $\alpha_{\rm AS}$. The crucial point about scales

JHEP08(2017)004

$\mu \approx \mu_{\rm AS}$ is that the two loop terms have become active. Two loop terms also contribute to the running of $\alpha_{\rm AF}$ and thereby ensure that the sign of $B'_{\rm AF}$ has become positive. We conclude that (4.10) is sufficient to provide an upper bound for viable matchings to the SM, ensuring that neither of the couplings escapes a successful matching through a Landau pole at intermediate energies. Within the confines of (4.10), this enables us to match SM and BSM running onto each other essentially at any scale between TeV and Planckian energies.

4.3 Fully interacting fixed points

All fully interacting UV fixed points are characterized by a stability matrix (2.8) with a single relevant eigenvalue. This important result states that a linear combination of the gauge groups' kinetic terms together with the BSM Yukawa interaction term in the fundamental Lagrangean (3.3) correspond to the sole UV relevant operator in the theory. This result has important implications. Unlike in asymptotically free theories (or in asymptotically safe theories at partially interacting fixed points FP_2 or FP_3) where every gauge coupling corresponds to a UV relevant direction, here, instead, the UV critical surface is of a lower dimensionality. This new effect is a consequence of competing gauge interactions in the UV. Most notably, it entails that the number of fundamentally independent parameters is reduced, leading to an enhanced level of predictivity.

In our models, the UV critical surface at fully interacting UV fixed points becomes one-dimensional, parametrised by a single free parameter. Consequently, only one out of the three couplings $(\alpha_3, \alpha_2, \alpha_y)$ may be considered as an independent variable. For FP_4, and without loss of generality we chose this to be α_3. The UV critical surface then uniquely determines the weak and the Yukawa coupling as functions of the strong coupling,

$$\alpha_i = F_i(\alpha_3) \qquad \text{for } i = 2, y\,. \tag{4.11}$$

Most importantly, the UV critical surface imposes a relation between the two gauge couplings which arises as a strict consequence of asymptotic safety at a fully interacting fixed point FP_4. We may then use the dimensionless parameter

$$\delta\alpha_3(\Lambda) = \alpha_3^* - \alpha_3(\Lambda) \tag{4.12}$$

at the high scale Λ to parametrise all UV safe trajectories running out of the fully interacting UV fixed point FP_4. The UV-IR connecting separatrix

$$(\alpha_3, \alpha_2, \alpha_y)(\mu) \equiv \big(\alpha_3, F_2(\alpha_3), F_y(\alpha_3)\big)(\mu) \tag{4.13}$$

uniquely determines the relation between the strong and the weak gauge coupling for all scales above the matching scale. The role of the free parameter $\delta\alpha_3(\Lambda)$ is to determine at which scale the curves (4.13) display a cross-over from UV dominated running towards IR dominated running. The task to identify trajectories which can be matched onto the SM at some matching scale $\mu = M$ reduces to analysing the separatrix (4.13). Given that the set of determining equations is over-constrained, a successful matching cannot be guaranteed from the outset, meaning that the viability needs to be checked for each FP_4. On the other

JHEP08(2017)004

hand, if trajectories emanating out of FP_4 can be matched, the BSM extension implies a fundamental relation between both gauge couplings, which would not exist otherwise. In settings where FP_4 exists alongside FP_2, or FP_3, or both, either of the partially interacting fixed points is the more relevant UV fixed point. Their UV critical dimensions are larger, UV-IR connecting trajectories can be found which link FP_2 or FP_3 with FP_4. An example for this is discussed below in figure 11.

To understand more explicitly how a matching of FP_4 onto the SM depends on the fermion representations and flavor multiplicities, we evaluate the link between the gauge couplings as dictated by the UV critical surface, (2.9). Since in the general case the separatrix cannot be resolved analytically, we use the critical surface approximation of (2.9), see appendix A for the technicalities, keeping in mind that far from the UV fixed point the critical surface may deviate from the one given by the separatrix. The relation (4.11) then takes the simple linear form

$$\begin{aligned} \alpha_2(M) &= -X + Y\,\alpha_3(M)\,, \\ Y &= -V_2/V_3\,, \\ X &= -\alpha_2^* + Y\,\alpha_3^*\,. \end{aligned} \tag{4.14}$$

The parameters V_i are related to the UV relevant eigendirection (2.9) which characterises the UV critical surface. Using (3.7), we find the explicit expressions

$$X = \frac{B_3 D_2 - B_2 D_3}{C_2 D_3 - G_3 D_2}\,, \qquad Y = \frac{C_3 D_2 - G_2 D_3}{C_2 D_3 - G_3 D_2}\,, \tag{4.15}$$

in terms of the perturbative loop parameters. Whether a matching of trajectories $(\alpha_2, \alpha_3)(\mu)$ with (4.14) onto the SM is possible or not depends on the signs and magnitude of X and Y. In the large-N_F limit, we find

$$\begin{aligned} X\big|_{N_F \gg 1} &= \frac{21}{5}\,\frac{C_2(R_2) - \frac{19}{112} C_2(R_3)}{C_2(R_3) C_2(R_2) d(R_3) d(R_2)}\,\frac{1}{N_F} + \text{subleading}\,, \\ Y\big|_{N_F \gg 1} &= \frac{3}{2} + \text{subleading}\,. \end{aligned} \tag{4.16}$$

With increasing N_F we observe that $Y > 0$ rapidly approaches the large N_F limit $Y = \frac{3}{2}$.[4] Conversely, X may have either sign depending on the representation (R_3, R_2), though not on N_F. Also, X becomes parametrically small for high dimensional representations and for large flavor multiplicities N_F. If $X < 0$ we have $\alpha_2(M) > \alpha_3(M)$ indicating that a matching below GUT-type scales is impossible. Furthermore, (4.14) also implies that $\alpha_2(M) > -X$, stating that a matching becomes impossible at any scale if $-X$ becomes too large. On the other hand, if $X > 0$ matchings can be found to SM values, in particular at low scales where $\alpha_2(M) < \alpha_3(M)$. For intermediate and large values of N_F the condition $X > 0$ becomes

$$C_2(R_2) - \frac{19}{112} C_2(R_3) > 0\,. \tag{4.17}$$

[4]Note that this ratio is a direct consequence of the $\mathrm{SU}(3)_C$ and $\mathrm{SU}(2)_L$ gauge groups of the SM.

JHEP08(2017)004

A few comments are in order:

(*i*) If $R_3 < \mathbf{10}$, the condition (4.17) is satisfied for any R_2. Non-trivial constraints arise from (4.17) once $R_3 = \mathbf{10}$ or higher (for example, $R_3 = \mathbf{10}$ necessitates $R_2 \geq \mathbf{3}$, and similarly for higher dimensional representations $R_3 > \mathbf{10}$).

(*ii*) An increasing flavor multiplicity N_F is required for models with a low dimensional $\mathrm{SU}(3)_C$ representation R_3 or high dimensional $\mathrm{SU}(2)_L$ representation R_2 to ensure that the magnitude of X stays within the limits compatible for a matching onto SM values. Also, increasing the dimension of the matter representations lowers $\alpha_3(M)$. For these cases it then follows that the matching can only take place at a high scale.

(*iii*) The linear approximation for the separatrix (4.14) becomes exact once $R_2 = \mathbf{1}$. This can be seen as follows. Using (4.15) we find $X = -\frac{19}{35}$ at FP_4 for any viable (R_3, N_F). The exact same result is found if (4.14) is evaluated at the Banks-Zaks IR fixed point of the weak gauge coupling in the SM $(\alpha_2^*, \alpha_3^*) = (\frac{19}{35}, 0)$, see (A.10). This result indicates that the UV critical surface (4.14) at FP_4 coincides with the critical surface at the Banks-Zaks IR fixed point. The latter therefore controls the running of the weak coupling away from the fully interacting UV fixed point by directing all UV safe trajectories straight into the Banks-Zaks fixed point. As is shown more explicitly below, it is for this reason that a matching of FP_4 with $R_2 = \mathbf{1}$ onto the SM is impossible.

(*iv*) For all scenarios considered in this work, we find that the condition (4.17) is a good estimator for the availability of a matching with the SM.

This completes the general discussion of matching conditions for UV safe trajectories onto the SM.

4.4 Benchmark scenarios

Let us now illustrate how the matching works in practice for a selection of benchmark scenarios, summarised in table 7, covering low scale and high scale matchings.

Benchmark scenario A. For this setting we assume that the BSM fermions do not carry $\mathrm{SU}(3)_C$ charges. Following on from our earlier discussion, FP_2 is the sole UV fixed point which may arise and neither FP_3 nor FP_4 are available, see figure 4. We consider the parameters

$$(R_3, R_2, N_F) = (\mathbf{1}, \mathbf{4}, 12) \tag{4.18}$$

with RG trajectories displayed in figure 6. The matching scale M may take any value between TeV and Planckian energies. In figure 6, for illustration, we have set it to the low value $M = 2\,\mathrm{TeV}$ (vertical dashed line). Evidently, the running of the strong coupling is not modified by BSM matter and remains SM-like throughout. Once the matching scale is fixed, the model predicts the value of the (otherwise unconstrained) Yukawa coupling. For $M = 2\,\mathrm{TeV}$ one obtains $\alpha_y(M) = 0.022$. We have also indicated the cross-over scale where the running of the asymptotically safe couplings changes from power-law behavior in

JHEP08(2017)004

Model	*Parameter* (R_3, R_2, N_F)	*UV fixed points* α_3^*	α_2^*	α_y^*	*Type* (figure 4)	*Info*
A	$(\mathbf{1}, \mathbf{4}, 12)$	0	0.2407	0.3385	$\mathbf{FP_2}$ ●	figure 6, low scale*
B	$(\mathbf{10}, \mathbf{1}, 30)$	0.1287	0	0.1158	$\mathbf{FP_3}$ ■	figure 7, low scale*
		0.1292	0.2769	0.1163	$\mathbf{FP_4}$ ♦	figure 8, no match
C	$(\mathbf{10}, \mathbf{4}, 80)$	0.3317	0	0.0995	$\mathbf{FP_3}$ ■	figure 9, low scale*
		0.0503	0.0752	0.0292	$\mathbf{FP_4}$ ♦	figure 10, high scale
		0	0.8002	0.1500	$\mathbf{FP_2}$ ●	Figure 11, high scale
D	$(\mathbf{3}, \mathbf{4}, 290)$	0	0.0895	0.0066	$\mathbf{FP_2}$ ●	(no figure), low scale*
		0.0416	0.0615	0.0056	$\mathbf{FP_4}$ ♦	figure 12, low scale
E	$(\mathbf{3}, \mathbf{3}, 72)$	0.1499	0.2181	0.0471	$\mathbf{FP_4}$ ♦	figure 13, low scale

Table 7. UV fixed points and matching characteristics for various benchmark scenarios. An asterisk indicates that a matching is permitted at any scale including low (TeV) energy scales.

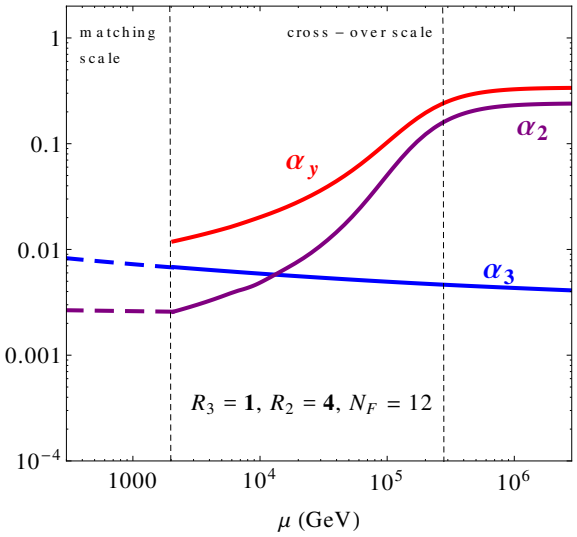

Figure 6. Low scale matching of the partially interacting fixed point FP_2 onto the SM for the benchmark scenario A with $(R_3, R_2, N_F) = (\mathbf{1}, \mathbf{4}, 12)$ and $M = 2\,\mathrm{TeV}$. BSM (SM) running is shown by full (dashed) lines. Around the cross-over scale the BSM running of α_2 and α_y slows down from power-law to logarithmic. Notice that the running of the strong coupling is not modified by BSM fermions.

the deep UV to logarithmic behavior towards the IR (dashed vertical line). The cross-over scale is found to be around $\mu_{\mathrm{cr}} \sim 3 \times 10^5\,\mathrm{GeV}$ and much larger than the matching scale.

Benchmark scenario B. For this case we assume that the BSM fermions do not carry $\mathrm{SU}(2)_L$ charges. From figure 4 it follows that solely FP_3, possibly in conjunction with FP_4 can arise. Informed by the results of tables 4 and 6 we chose the parameters

$$(R_3, R_2, N_F) = (\mathbf{10}, \mathbf{1}, 30) \tag{4.19}$$

JHEP08(2017)004

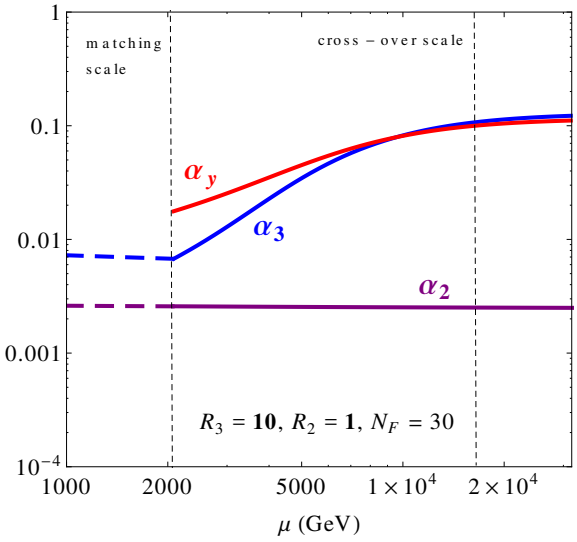

Figure 7. Low scale matching from the partially interacting fixed point FP_3 onto the SM for the benchmark scenario B with $(R_3, R_2, N_F) = (\mathbf{10}, \mathbf{1}, 30)$ and $M = 2\,\mathrm{TeV}$. BSM (SM) running is shown by full (dashed) lines. Around the cross-over scale the BSM running of α_3 and α_y slows down from power-law to logarithmic. Notice that the running of the weak coupling is not modified by the BSM fermions.

to ensure that the model has both types of UV fixed points, FP_3 and FP_4. The partially interacting fixed point FP_3 can always be matched onto the SM at any scale. In figure 7, this is illustrated for a low matching scale $M = 2\,\mathrm{TeV}$. In this model, the running of the weak gauge coupling is not modified by BSM matter to the leading orders in perturbation theory. The crossover scale $\mu_{\mathrm{cr}} \sim 1.6 \times 10^4\,\mathrm{GeV}$ is an order of magnitude larger than the matching scale. Elsewise the same reasoning as in figure 6 applies. In contrast, the impossibility for a matching at FP_4 is illustrated in figure 8. The scale μ_0 is arbitrary and can take any value upon tuning the UV parameter $\delta\alpha_3(\Lambda)$. However, the UV safe trajectory emanating out of FP_4 is attracted towards the strongly coupled domain, owing to the Banks-Zaks IR fixed point at $(\alpha_2^*, \alpha_3^*) = (\frac{19}{35}, 0)$ in the weak sector, (A.10). Consequently, the weak coupling cannot become weak in the IR and a matching to SM values is impossible at any intermediate scale due to the dominance of the Banks-Zaks fixed point. We stress that this pattern is a direct consequence of the BSM fermions being uncharged under $\mathrm{SU}(2)_L$. The non-availability of FP_4 persists for all models with $R_2 = \mathbf{1}$, in line with our discussion in section 4.3.

We now turn to benchmark scenarios where the BSM fermions carry both $\mathrm{SU}(2)_L$ and $\mathrm{SU}(3)_C$ charges. In these cases we find realisations for either of the partially interacting fixed points FP_2 and FP_3, as well as for the fully interacting fixed point FP_4.

Benchmark scenario C. As soon as $R_2 \geq \mathbf{2}$ and $R_3 \geq \mathbf{3}$, and for sufficiently large N_F, all three types of UV fixed points arise, see figure 4. To illustrate such settings, we consider

JHEP08(2017)004

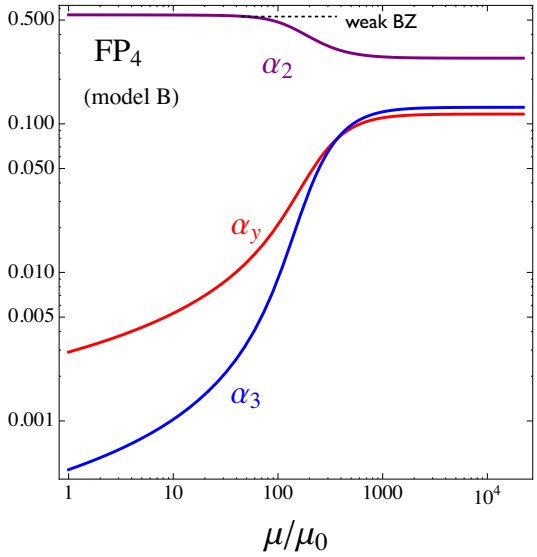

Figure 8. Shown is the running of the gauge and BSM Yukawa couplings along the UV-IR connecting separatrix emanating from FP_4 for the benchmark model B, (4.19). The scale μ_0 may take any value determined by the free parameter $\delta\alpha_3(\Lambda)$. The weak gauge coupling is attracted towards its "would-be" Banks-Zaks fixed point (weak BZ) , see (A.10), indicated by the dashed line. Consequently, the interacting UV fixed point cannot be matched onto the SM.

the benchmark scenario C with parameters

$$(R_3, R_2, N_F) = (\mathbf{10}, \mathbf{4}, 80) \tag{4.20}$$

which displays FP_2, FP_3 and FP_4 within the perturbative domain, see table 7. In figure 9, we begin with FP_3 where $\alpha_2^* = 0$ in the deep UV. Once more we observe that the matching condition (4.10) on the one loop BSM parameters for the strong and the weak coupling can be satisfied at any scale between a few TeV and Planckian energies including the low matching scale $M = 2\,\mathrm{TeV}$ chosen in figure 9. Furthermore, the weak coupling α_2 continues to decrease even directly below the matching scale, for any matching scale. For the weak gauge coupling the approach towards asymptotic freedom is accelerated over the SM rate owing to the two loop BSM Yukawa contributions which are winning over the contributions by the strong gauge coupling along the entire UV-IR connecting separatrix into the fixed point. This pattern is consistent with the matching condition (4.10), which is fullfilled for any intermediate scale. For the example shown in figure 9, the cross-over scale and the matching scale are separated by an order of magnitude.

In figure 10 we turn to the matching of the fully interacting fixed point FP_4 corresponding to the same parameter set (4.20). Couplings run out of the UV fixed point FP_4 along a unique separatrix (4.13) connecting FP_4 with the Gaussian fixed point. The separatrix thereby imposes a link between α_2 and α_3. On the separatrix, and close to the fully interacting fixed point, the weak coupling is genuinely stronger than the strong coupling. At crossover, it becomes rapidly weaker than the strong coupling. The gauge couplings also weaken more rapidly than the BSM Yukawa coupling. For the parameters (4.20), the

JHEP08(2017)004

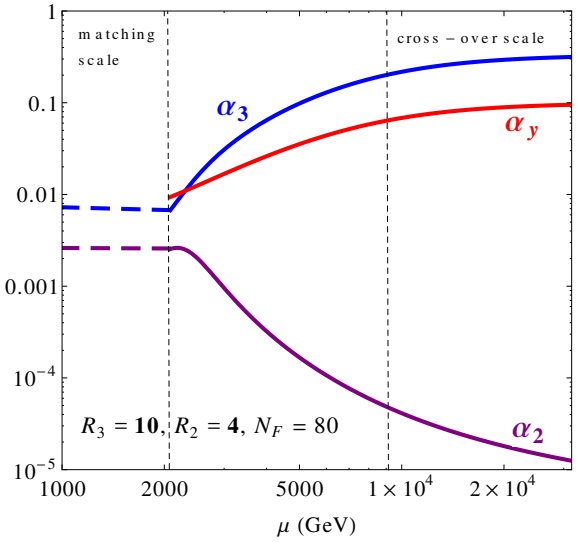

Figure 9. Low scale matching from the partially interacting fixed point FP_3 onto the SM for the benchmark scenario C with $(R_3, R_2, N_F) = (\mathbf{10}, \mathbf{4}, 80)$ and $M = 2\,\mathrm{TeV}$. BSM (SM) running is shown by full (dashed) lines. Around the cross-over scale the BSM running of α_3 and α_y slows down from power-law to logarithmic. Notice that the approach towards asymptotic freedom of the weak coupling is enhanced by BSM fermions.

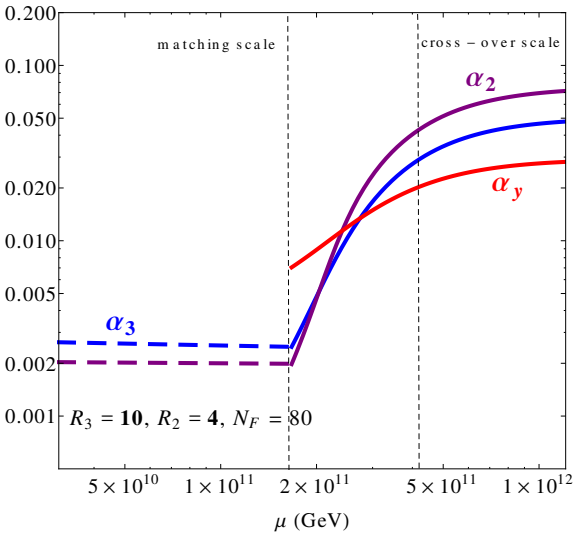

Figure 10. High scale matching of a fully interacting fixed point FP_4 onto the SM for the benchmark scenario C with $M = 2 \times 10^{11}\,\mathrm{GeV}$. Once BSM matter fields are active, the weak coupling approaches asymptotic safety more rapidly than the strong coupling. See also figure 9 and figure 11.

separatrix dictates that the unique matching scale onto SM values comes out comparatively high, with $M \approx 2 \times 10^{11}\,\mathrm{GeV}$.

In figure 11 we consider the matching with FP_2 where $\alpha_3^* = 0$ in the UV. In this model, we find that a matching at FP_2 is more strongly constrained compared to a generic

JHEP08(2017)004

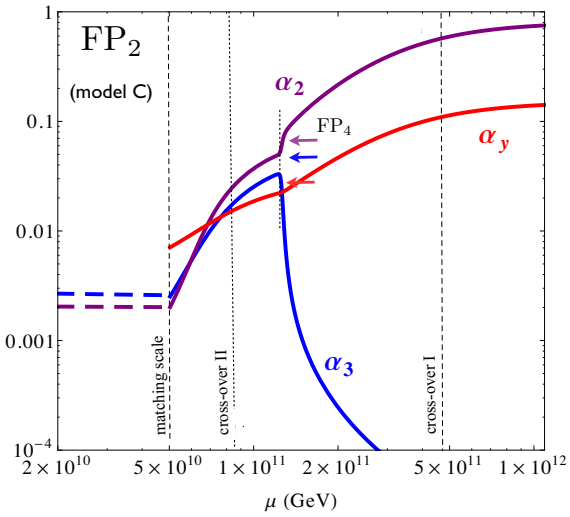

Figure 11. High-scale matching of a partially interacting fixed point FP_2 onto the SM for the benchmark scenario C with $(R_3, R_2, N_F) = (\mathbf{10}, \mathbf{4}, 80)$. Trajectories emanate out of the UV fixed point FP_2 and initially cross over into the vicinity of FP_4 (indicated by arrows) at around $1.5 \times 10^{11}\,\mathrm{GeV}$. Subsequently, trajectories display a second cross over to match with the SM at about $M = 5 \times 10^{10}\,\mathrm{GeV}$.

partially interacting fixed point. The reason for this is the influence of FP_4 on UV-IR connecting trajectories and the necessity to avoid an early Landau pole in the strong sector. Specifically, starting at some high scale Λ we observe that the weak and the Yukawa couplings decrease with energy, while the strong coupling increases towards the IR. For too small $\delta\alpha_3(\Lambda)$ (4.5) the strong coupling does not grow fast enough. For too large $\delta\alpha_3$ the strong coupling runs into a Landau pole at intermediate scales. Within a narrow window for $\delta\alpha_3$, however, the growth of α_3 is tamed due to FP_4. Then, trajectories are close to the separatrix connecting FP_2 with FP_4, with a cross-over scale $\mu \approx 5 \times 10^{11}\,\mathrm{GeV}$, see figure 11. Below the cross-over scale, couplings are attracted towards FP_4 (see table 7 for the fixed point values) which, however, is not reached exactly. Instead, at scales about $\mu \approx 1.2 \times 10^{11}\,\mathrm{GeV}$ the couplings are driven away from FP_4, now following the separatrix which connects FP_4 with the Gaussian. In consequence, we find that couplings can be matched onto the SM at a high matching scale of about $M = 5 \times 10^{10}\,\mathrm{GeV}$, close to the matching scale found for FP_4.

This result is consistent with the "Landau pole avoidance condition" (4.10) derived in section 4.2, which for the parameters (4.20) has no solutions for low matching scales. For example, at $M = 2\,\mathrm{TeV}$ the SM predicts $\alpha_3^{\mathrm{SM}}(M) \approx 0.0067$, yet the upper boundary (4.10) reads $\alpha_3(M) \approx 0.004$. Only for sufficiently high matching scales such as $M \approx 5 \times 10^{10}\,\mathrm{GeV}$, the condition (4.10) eases up and allows a consistent matching without the strong coupling prematurely running into a perturbative Landau pole at intermediate scales.

We conclude that all three fixed points qualify as UV completions for the SM, although the specifics of the UV completion differ due to finer details of the fixed point structure.

JHEP08(2017)004

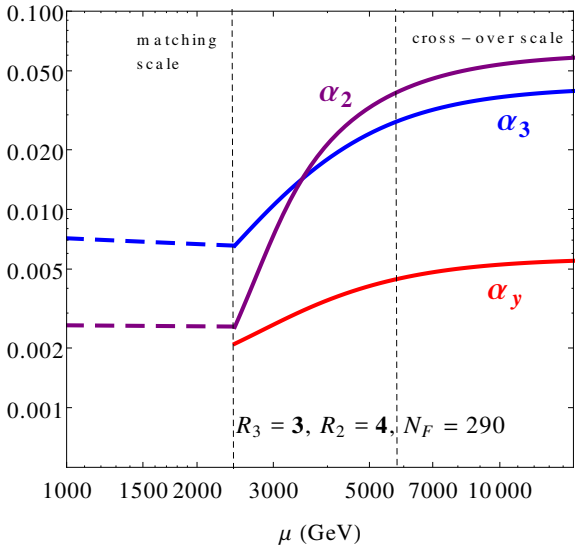

Figure 12. Low scale matching from the fully interacting fixed point FP_4 onto the SM for the benchmark scenario D with $(R_3, R_2, N_F) = (\mathbf{3}, \mathbf{4}, 290)$ and matching scale $M = 2.4\,\mathrm{TeV}$. Once BSM matter fields are active, the weak coupling approaches asymptotic safety more rapidly than the strong coupling.

Benchmark scenario D. For models with $R_3 = \mathbf{3}$ and $R_2 \geq \mathbf{3}$, and for sufficiently large N_F, we have observed that the UV fixed points FP_2 and FP_4 coexist, see figure 4. To illustrate the matching procedure for these settings, we set the parameters as

$$(R_3, R_2, N_F) = (\mathbf{3}, \mathbf{4}, 290)\,. \tag{4.21}$$

The partially interacting fixed point FP_2 can be matched onto the SM, particularly at low matching scale M (not displayed). Results for FP_4 are displayed in figure 12. Couplings run out of the UV fixed point along the separatrix (4.13). Unlike the previous example of benchmark C (4.20), in this case couplings display a cross over at much lower energies. In particular, a matching to SM values is possible at a low scale of about $M \approx 2.4\,\mathrm{TeV}$. As explained after (4.15), the price to pay is the necessity for a large multiplicity of flavors, significantly larger than $N_{\mathrm{AS}} = 18$ as minimally required for weakly coupled asymptotic safety to arise (see table 6). It is worth contrasting the successful matching at FP_4 with the failure for the benchmark scenario B (4.19): unlike the weak sector of the SM, the strong sector does not display a "would-be" Banks Zaks IR fixed point, see (A.9). Consequently, trajectories emanating out of FP_4 are attracted towards the Gaussian fixed point rather than being diverted by an interacting fixed point as in (4.19). We conclude that the (non)-availability of a matching with FP_4 in the benchmark scenario D (B) is dictated by features of the SM rather than the specifics of the BSM extension.

Benchmark scenario E. For all settings with $R_2 \geq \mathbf{2}$ and $R_3 \geq \mathbf{3}$, the theory can display all three types of interacting UV fixed points. In any of these cases, FP_4 arises at the lowest possible value for N_F, see figure 4. It is then interesting to evaluate scenarios

JHEP08(2017)004

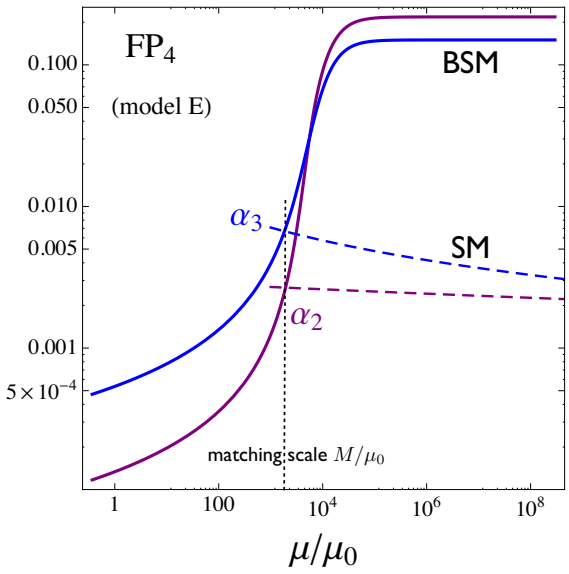

Figure 13. The matching procedure at FP_4 for the benchmark model E with parameters (4.22). The thick lines show the BSM running along the UV-IR connecting separatrix as a function of the scale μ_0, which may take any value determined by the free parameter $\delta\alpha_3(\Lambda)$. The dashed lines show the SM running of couplings from figure 5 provided that $\mu_0 = 1\,\mathrm{GeV}$. It is observed that SM and BSM values both coincide at the matching scale $M \approx 1.6\,\mathrm{TeV}$, see (4.2), indicated by the short-dashed vertical line.

where FP_4 is the sole UV fixed point. Using our results from table 6 we consider exemplarily the case

$$(R_3, R_2, N_F) = (\mathbf{3}, \mathbf{3}, 72)\,. \tag{4.22}$$

The UV-IR connecting separatrix is displayed in figure 13. We observe that both gauge couplings decrease towards the IR. The scale μ_0 is a free parameter and solely fixed by the free parameter $\delta\alpha_3(\Lambda)$ in the deep UV. We confirm once more that the hierarchy $\alpha_2 > \alpha_3$ in the deep UV invariably transforms into $\alpha_2 < \alpha_3$ once the RG flow falls below the cross-over scale. Also shown is the SM running of gauge couplings (dashed lines) taken from figure 5, with data points starting from $\mu = 1\,\mathrm{TeV}$ (corresponding to the choice $\mu_0 = 1\,\mathrm{GeV}$ on the lower axis). Tuning the value of $\delta\alpha_3(\Lambda)$ (or μ_0) along the separatrix amounts to shifting the separatrix in its entirety parallel to the lower axis. In figure 13, values have been chosen to exemplify that the separatrix can match SM values, (4.2), at the matching scale $M \approx 1.6\,\mathrm{TeV}$. We stress once more that the shape of the separatrix, and hence the fixed point behavior of the theory in the deep UV, uniquely dictates the scale at which a matching to the SM can be made.

4.5 Synopsis of matching conditions

To summarise, we have established that partially interacting fixed points FP_2 and FP_3 can comfortably be connected with the SM at low energies provided there are no nearby competing fixed points in the phase diagram of the theory. Moreover, in these cases the

JHEP08(2017)004

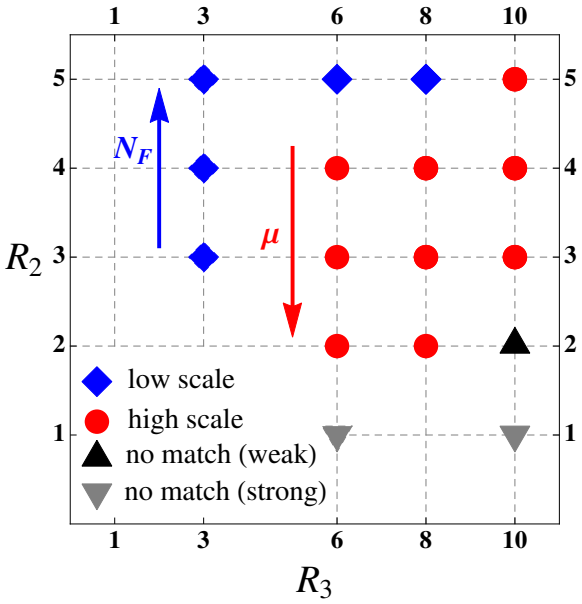

Figure 14. Summary of matching conditions at fully interacting UV fixed points FP_4 of the RG system (3.7) in dependence on the BSM parameters (R_3, R_2, N_F). Blue diamonds indicate low-scale matchings in the multi-TeV regime. Red dots stand for a high matching scale beyond the reach of present day colliders. Black triangles indicate scenarios where a matching onto SM values is not available despite of both gauge couplings approaching the Gaussian. Gray triangles indicate the unavailability of a matching due to strong coupling phenomena in the weak gauge sector ($R_2 = \mathbf{1}$). Arrows additionally illustrate how the number of BSM fermion flavors N_F (blue arrow) and the matching scale μ (red arrow) vary with the representation to ensure a successful matching.

matching scale and thus the masses of BSM matter fields remain freely adjustable parameters. The underlying reason for this is that both gauge couplings remain relevant couplings in the deep UV. Typical examples for this are shown in figure 6, 7, and 9 for FP_2 of benchmark A, and FP_3 of benchmark B and C, respectively. On the other hand, a matching to the SM becomes more contrived, or even impossible, if nearby competing fixed points influence the running of couplings. An example for this is shown in figure 11 for FP_2 of benchmark C, where the nearby fully interacting fixed point FP_4 impacts on the UV-safe trajectories emanating out of the partially interacting fixed point FP_2, thereby enforcing a high matching scale.

The matching of fully interacting fixed points FP_4 to the SM is qualitatively different. The reason for this is that only one of the gauge couplings remains a relevant coupling, which reduces the number of freely adjustable parameters in the UV by one. Unlike partially interacting ones, fully interacting fixed points predict a relation between the gauge couplings. The availability of a matching to the SM is then encoded in the UV-IR connecting separatrix and must be checked on a case by case basis, see figure 12. In figure 14 we summarise our results for the matching conditions at FP_4 in dependence on the BSM paramaters (R_3, R_2, N_F). Low-scale matchings in the multi-TeV regime are indicated by blue diamonds. Examples for this relate to benchmark D and E displayed in figure 12

JHEP08(2017)004

and 13, respectively. This is contrasted with matchings at a high scale, beyond the reach of present day colliders (red dots). An example for the latter is furnished by benchmark C as shown in figure 10. On the other hand, matchings fail if gauge couplings along the separatrix never hit SM values, figure 5, despite both gauge couplings approaching the Gaussian. In figure 14 such scenarios are indicated by black triangles. Finally, nearby competing fixed points may distort the UV-safe separatrix and disallow a matching to the SM. In figure 14, the unavailability of matching due to strong coupling in the weak gauge sector ($R_2 = \mathbf{1}$) is indicated by gray triangles. An example for this is benchmark B in figure 8 where the competing fixed point is the "would-be" Banks-Zaks fixed point of the SM weak sector. Arrows have been added in figure 14 to illustrate how the number of BSM fermion flavors N_F (blue arrow) and the matching scale μ (red arrow) vary with the BSM matter representation to ensure a successful matching.

We briefly come back to the perturbativity of interactions in the fixed point regime. We have found that the gauge couplings for all benchmarks take small values $\alpha \approx 0.04$–0.8, see table 7. Moreover, in the large-N_F and large representation limit, fixed point couplings are parametrically small, (3.20)–(3.25). In models which permit an asymptotic large-N Veneziano limit, it has also been shown that perturbativity in $N_F \cdot \alpha \ll 1$ is guaranteed [12]. Here, at finite N_F, the products $N_F \cdot \alpha$ come out of order $\mathcal{O}(1$–$10)$ for all benchmarks, hinting towards the onset of strong coupling. Ultimately, this pattern of result reflects the unavailability of a Veneziano limit because fixed points necessitate representations higher than the fundamental, figure 4. Future studies should therefore include loop corrections beyond the leading orders, and non-perturbative effects.

Finally, we comment on the role of the $\mathrm{U}(1)_Y$ hypercharge. The SM predicts a Landau pole for the hypercharge many orders of magnitude beyond the Planck scale $M_{\mathrm{Pl}} \sim 10^{19}\,\mathrm{GeV}$. In our setup the BSM fields do not carry hypercharge. The interesting case where BSM fields carry hypercharge will be detailed elsewhere. Nevertheless, the running of the hypercharge nevertheless differs from SM running above the matching scale because the strong or the weak or both gauge coupling(s) will grow and eventually settle at interacting fixed points. Interacting fixed points accelerate the running of the hypercharge due to contributions at two loop. To exclude that a Landau pole may arise below Planckian energies, we assume a "worst case" scenario in which (α_2, α_3) take fixed point values already at a very low scale of 1.5 TeV (bounds are softened if fixed point values are reached at higher scales). This leads to a conservative exclusion plot shown in figure 15 where the shaded area indicates the forbidden region of values for the UV fixed point. We observe that gauge sectors must become strongly coupled already at low energies to inflict a Landau pole below Planckian energies for the hypercharge. For comparison, we also indicate the location of UV fixed points for the benchmark models A, B, C, D and E as given in table 7. Quantitatively, none of the benchmark models reach a Landau pole for the hypercharge below $10^{26}\,\mathrm{GeV}$. We conclude that all benchmark models are deeply in the UV-safe region of parameter space.

JHEP08(2017)004

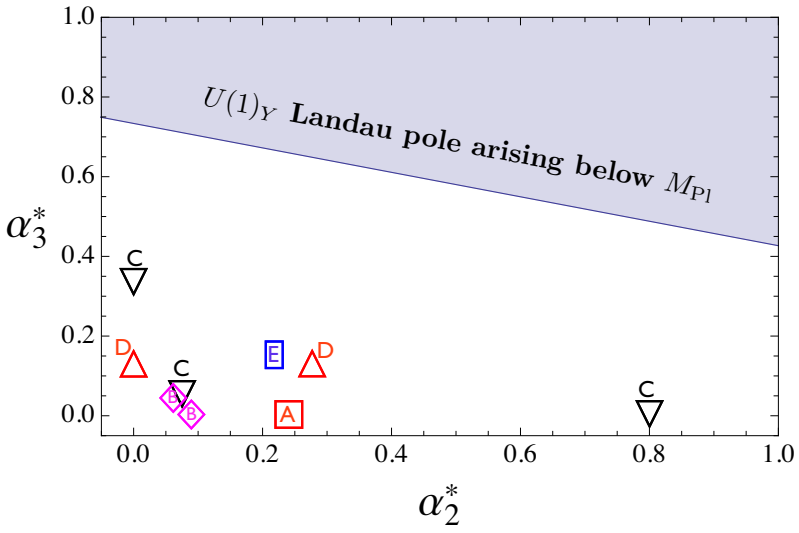

Figure 15. Shown is a conservative estimate for the exclusion area (gray) of fixed point values for the gauge couplings (α_2, α_3) to ensure the absence of a Landau pole for the $\mathrm{U}(1)_Y$ hypercharge below Planckian energies. Equally shown are the partially and fully interacting fixed point values for the benchmark models A, B, C, D and E given in table 7, for comparison. All benchmark models are UV-safe.

5 Phenomenology

In this section we discuss experimental signatures of asymptotically safe SM extensions. We assume that the BSM sector can at least partially be accessed at the LHC, which implies a low matching scale and masses of the BSM matter fields in the multi-TeV range. An order of magnitude heavier states can be considered at future colliders [23]. Because of the flavor symmetry the BSM fermions are stable in the model (3.3). Allowing the flavor symmetry to be broken, the lightest BSM fermion is still stable as long as Yukawa interactions with SM fermions are absent. The latter holds except for a few low-dimensional representations with tuned hypercharge of the BSM fermions. As we assume that the BSM fields do not carry hypercharge, these exceptional cases cannot be realized. Without mixing with SM fermions, flavor physics constraints are not relevant to our models. We further assume $R_3 \neq \mathbf{1}$. If the new fermions would be colorless, their production at hadron colliders would be of higher order and suppressed. Scenarios with $R_3 = \mathbf{1}$ are certainly suitable for study at an e^+e^--machine operating at high energies [23–25].

An obvious search strategy is to look for asymptotically safe BSM physics by probing the strong running coupling evolution and the weak interaction. We discuss various constraints and opportunities from the running gauge couplings, from the weak sector, from direct searches for long-lived QCD-bound states composed out of BSM fermions and SM partons, and from LHC diboson searches, offering further constraints on BSM matter including the (M_ψ, M_S) parameter space.

JHEP08(2017)004

5.1 Strong coupling constant evolution

The presence of a large number of fermions charged under $\mathrm{SU}(3)_C \times \mathrm{SU}(2)_L$ changes the running of the corresponding gauge couplings drastically, as illustrated in figures 6–13. The deviation from the SM, shown in figure 5, kicks in rather quickly with an order one increase in slope of the asymptotically safe coupling and provides a smoking gun signature of BSM physics considered in this work. Threshold corrections are not expected to change this picture qualitatively, although the onset of BSM effects may be somewhat smoother.

The CMS collaboration has extracted the value of the QCD running coupling up to the scale 2 TeV [26] using the measurement of the inclusive jet cross section for proton-proton collisions at a centre-of-mass energy of 7 TeV with data corresponding to an integrated luminosity of $5.0\,\mathrm{fb}^{-1}$ [27]. This determination is consistent with the SM. Also other measurements, including the one of the inclusive 3-jet production differential cross section [28], have not observed deviations from the two-loop running predicted in the SM up to 1.5 TeV. Therefore, modulo threshold corrections, the lower limit on the mass of new colored matter reads

$$M_\psi \gtrsim 1.5\,\mathrm{TeV}. \tag{5.1}$$

In the following subsections we work out further experimental constraints on M_ψ, which in turn imply limits on the matching scale. We recall that scenarios with partially interacting fixed points FP_2 and FP_3 can generically be matched at any scale (except in specific circumstances, see figure 11), whereas the matching scale is uniquely fixed for fully interacting fixed points FP_4. The latter scenarios are therefore subject to stronger experimental constraints.

In figure 16 we show the running of the strong coupling (black dashed line) and its uncertainty (green band) as determined by CMS [26]. In addition, we show the running of α_3 in the asymptotically safe benchmarks B, C and E introduced in table 7 for low matching scales around 1.5 to 2 TeV. Note that benchmark E (blue curve) relates to a fully interacting UV fixed point whose matching scale is fixed at 1.6 TeV. As can be seen, benchmark E is already being probed experimentally. Threshold corrections may allow to evade the CMS limit, as the data near 2 TeV are also losing statistics.

5.2 The weak sector

The experiments at the LEP collider have probed the SM's electroweak sector with scrutiny and found no significant deviation up to ~ 209 GeV [29]. The LHC has extended related SM tests into the several $\mathcal{O}(100)$ GeV regime [30], still allowing for weakly-interacting uncolored vector-like fermions below the TeV-scale. Within asymptotically safe models, this can happen, for instance, in benchmark A by noting that since the fixed point is partial only, the matching scale can be different than the one shown in figure 6. Electroweak vector boson scattering at the LHC and at future lepton colliders [25] is sensitive to such BSM effects.

For $R_2 \neq \mathbf{1}$ contributions to the ρ-parameter arise if the BSM fermions encounter $\mathrm{SU}(2)_L$ breaking due to mass splitting $\delta M \ll M_\psi$ in the fermion multiplet. This implies [22]

$$N_F\, d(R_3)\, S_2(R_2)\, \delta M^2 \lesssim (40\,\mathrm{GeV})^2, \tag{5.2}$$

a splitting below percent level for TeV-ish fermion masses and higher.

JHEP08(2017)004

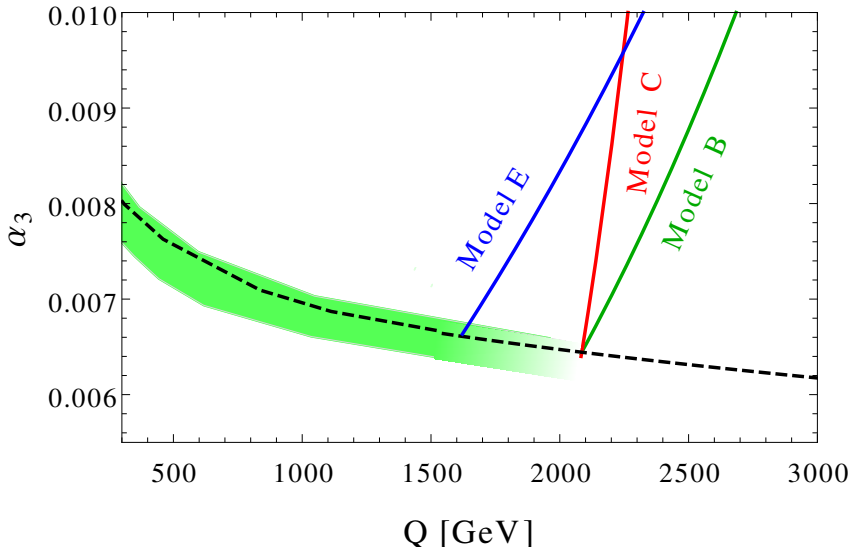

Figure 16. SM running of the QCD coupling constant (black dashed line) and its uncertainty (green band) as determined by CMS [26]. Colored solid lines indicate the running of α_3 in asymptotically safe benchmark scenarios B, C and E summarized in table 7 with a low matching scale around 1.5 to 2 TeV.

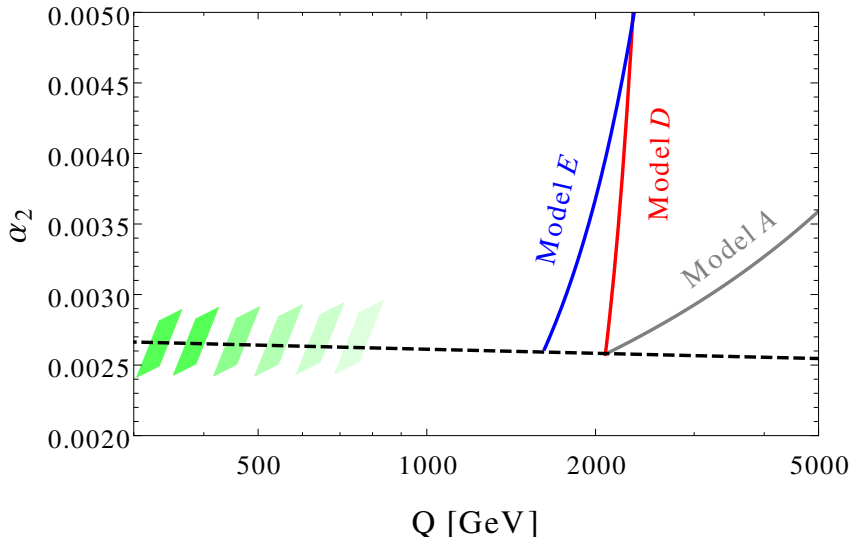

Figure 17. SM running of the weak coupling constant (black dashed line) and schematically indicated by the green hatched band the region where the weak sector of the SM has passed experimental tests, see text for details. Colored solid lines indicate the running of α_2 in asymptotically safe benchmark scenarios introduced in table 7 that allow for a low matching scale around 1.5 to 2 TeV.

In figure 17 we show the running of the weak coupling (black dashed line) and, schematically, the region with agreement with the SM's weak theory denoted by the hatched green band. The solid colored lines correspond to the asymptotically safe benchmarks A, D and E summarized in table 7 for a low matching scale around 1.5 to 2 TeV.

JHEP08(2017)004

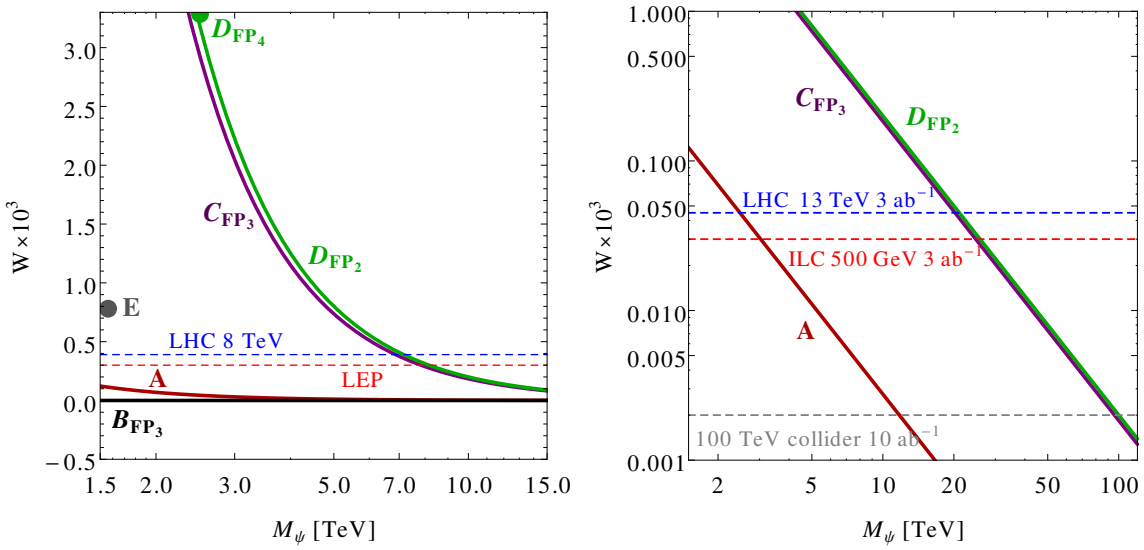

Figure 18. Shown is the electroweak precision parameter W (5.4) as a function of the BSM fermion mass for the low-scale benchmark models given in table 7. In the left panel dashed lines show 95% C.L. upper limits obtained from LEP (red) and the LHC at 8 TeV (blue). In the right panel dashed lines indicate the projected reach of the LHC at 13 TeV (blue), the ILC 500 GeV (red), and a 100 TeV collider (gray). Experimental limits are taken from [34].

Constraints from rare decays can be evaded as long as the BSM fermions do not couple directly to SM Higgs, quarks, or leptons — as is the case in our setup. For BSM fermions with $R_2 > \mathbf{1}$ a contribution to the anomalous magnetic moment of the muon arises at 2-loop in the electroweak interactions. We estimate this as $\Delta a_\mu \sim d(R_3)\, S_2(R_2)\, N_F\, [\alpha/(4\pi)(m_\mu/M_\psi)]^2$. Comparison with data $\Delta a_\mu^{\text{exp}} \sim (2\text{–}3)\cdot 10^{-9}$ [22] yields the constraint

$$d(R_3)\, S_2(R_2)\, N_F \left(\frac{\text{TeV}}{M_\psi}\right)^2 \lesssim 10^4, \tag{5.3}$$

which is satisfied for all our benchmarks in table 7 and for M_ψ above a TeV.

Below the BSM mass threshold the effects of the BSM fermions can be studied indirectly through electroweak precision tests. Charged and neutral current Drell-Yan (DY) processes offer a promising way to test such corrections [31], as they are both experimentally clean and very well understood theoretically. The oblique parameter W [32, 33] is of particular interests since its impact increases with energy allowing high precision studies at present and future colliders [34]. W is directly related to the BSM contribution that modifies the electroweak beta function,

$$W = -\frac{\alpha_2}{10}\,\frac{M_W^2}{M_\psi^2}\, B_2^{\text{BSM}}, \tag{5.4}$$

where B_2^{BSM} denotes the BSM contribution to the 1-loop coefficient B_2 of β_2, see A.2.

Figure 18 displays W versus the matching scale M_ψ for the benchmark scenarios defined in table 7. In the left panel the experimental 95% C.L. upper limits [34] from LEP (red

JHEP08(2017)004

dashed line) and LHC 8 TeV (blue dashed line) are shown. Constraints on negative W exist but are not relevant here. For the fully-interacting fixed points FP_4 of benchmark D and E (full dot), a low matching scale at around 2 TeV dictates a high multiplicity of BSM fermions, and a large contribution to (5.4). These scenarios turn out to be excluded. For scenarios with partially interacting fixed points (FP_2 or FP_3) the matching scale is a free parameter. For benchmark models C (magenta line) and D (green line) the matching scale must be larger than about 8 TeV to satisfy LEP constraints. Benchmark A (red line) is not yet constrained by the data owing to the low number of BSM fermion species N_F, while benchmark B (black line) is not probed at this order because its BSM fermions are $\mathrm{SU}(2)_L$ singlets.

The right panel of figure 18 shows the projected sensitivities of the LHC at 13 TeV with $3\,\mathrm{ab}^{-1}$ integrated luminosity (dashed blue line), the ILC 500 with $3\,\mathrm{ab}^{-1}$ (dashed red line), and a 100 TeV collider with $10\,\mathrm{ab}^{-1}$ (dashed gray line). The precision of the W determination is expected to increase by two orders of magnitude, requiring the matching scale in all allowed benchmark scenarios to be above around 10 TeV.

While this analysis demonstrates the importance of DY measurements for the type of BSM scenarios outlined here, constraints based on (5.4) must be taken with a grain of salt. The reason for this is that the corrections to W are only known to one loop order. In our framework, competing two loop corrections in the gauge beta functions play an important role as they are responsible for the fixed point. To estimate two loop effects, we replace B_2^{BSM} in (5.4) by the effective coefficient B_2' evaluated on the RG trajectory near the matching scale. For benchmark models C where α_3 becomes asymptotically safe, we find that the bound on the matching scale softens, from about 8 TeV to about 5 TeV. Also, benchmark B now contributes negatively to W and can be probed in the future. Similar two loop effects are expected for the other benchmark models. A complete two loop analysis of the oblique parameter W, although desirable, is beyond the scope of this work.

5.3 *R*-hadrons

We assume that at least some of the BSM fermions can be pair-produced,

$$2M_\psi < \sqrt{s}\,, \tag{5.5}$$

where $\sqrt{s}$ denotes the accessible center of mass energy at the collider. At least the lightest of the fermions has a long life, longer than a typical hadronization time scale, and forms colorless QCD bound states with ordinary partons (quarks and gluons), the so-called R-hadrons.

Both the ATLAS and CMS collaborations searched for heavy long-lived charged R-hadrons using a data sample corresponding to $3.2\,\mathrm{fb}^{-1}$ of proton-proton collisions at $\sqrt{s} = 13\,\mathrm{TeV}$. No significant deviations from the expected background have been observed which allowed to put a model-independent 95% confidence level (C.L.) upper limits on the production cross section of long-lived R-hadrons. In the framework of supersymmetry, those results have been translated into a lower bound on the mass of the fermionic partner of the gluon (gluino), which read 1.5 TeV for CMS [35] and 1.6 TeV for ATLAS [36].

JHEP08(2017)004

$\psi(R_3, R_2)$	$R_2 = 1$		$R_2 = 2$		$R_2 = 3$	
R_3	$\mathcal{C}_3$	$M_\psi^{\min}$ (TeV)	$\mathcal{C}_3$	$M_\psi^{\min}$ (TeV)	$\mathcal{C}_3$	$M_\psi^{\min}$ (TeV)
3	$5\frac{1}{3}$	(1.3)	$10\frac{2}{3}$	(1.4)	16	1.5
6	$66\frac{2}{3}$	1.7	$133\frac{1}{3}$	1.8	200	1.9
8	72	1.7	144	1.8	216	1.9
10	360	2.0	720	2.1	1080	2.2
15	$426\frac{2}{3}$	2.0	$853\frac{1}{3}$	2.1	1280	2.2
15′	$1306\frac{2}{3}$	2.2	$2313\frac{1}{3}$	2.3	3920	2.4

Table 8. Lower limits on the mass of the lightest BSM fermion, $M_\psi^{\min}$, as derived from the searches for long-lived charged particle by CMS [35, 37] and ATLAS [36] for $N_F = 1$. We make explicit a dependence on the fermion representations R_2 and R_3 under $\mathrm{SU}(2)_L$ and $\mathrm{SU}(3)_C$, respectively. The dominant contribution to the production cross section is proportional to $\mathcal{C}_3$, (5.6), which is also given. Values in parentheses correspond to scenarios (R_3, R_2) with no weakly interacting UV fixed points, see figure 4.

Recently CMS has updated their analysis to $12.9\,\mathrm{fb}^{-1}$ of data [37], with the corresponding limit on the gluino mass increased to 1.7 TeV.

At the LHC any colored and hypercharge-neutral BSM fermion would be produced in the same way. Therefore one can easily recast the experimental limits for gluino searches in the framework of asymptotically safe scenarios considered in this study. In the leading order the $\psi\bar{\psi}$ pairs can be produced by gluon fusion or by quark-anti-quark annihilation, where the former mechanism is a dominant one. We can additionally assume that the main contribution to $pp \to \psi\bar{\psi}$ comes from a t-channel exchange of a BSM fermion. In this case the production cross section $\sigma_{\psi\bar{\psi}}$ depends on (R_3, R_2, N_F) and scales proportionally to the factor $\mathcal{C}_3$,

$$\sigma_{\psi\bar{\psi}} \sim N_F\, \mathcal{C}_3 \quad \text{with} \quad \mathcal{C}_3 = [C_2(R_3)]^2\, d(R_3)\, d(R_2)\,. \tag{5.6}$$

We can then put lower limits on the BSM fermion mass using the experimental limits for gluinos provided in [35] and [36], rescaling the gluino production cross section by $\mathcal{C}_3$. Notice also that it is possible for real representations, such as those with (p, p) for R_3, that ψ is a Majorana fermion; in all other cases we ignore the differences with respect to the gluinos in our estimates.

In table 8 we show the lower bounds on M_ψ in dependence of R_2 and R_3 together with $\mathcal{C}_3$ for $N_F = 1$. The lower bound increases with increasing $d(R_3)$. For $R_3 = \mathbf{15'}$ and $d(R_2) > 1$ it reads 2.3 TeV. We conclude that colored BSM fermions must be heavier than at least 1.5 TeV, consistent with (5.1). For larger N_F, the bounds get stronger. For example, for benchmarks B, D and E defined in table 7 we find $M_\psi^{\min} = 2.6, 2.4$ and 2.1 TeV, respectively. The limit for benchmark C is beyond 2.8 TeV. For benchmarks C and D the constraints from DY processes obtained in section 5.2 are stronger than the R-hadron ones.

JHEP08(2017)004

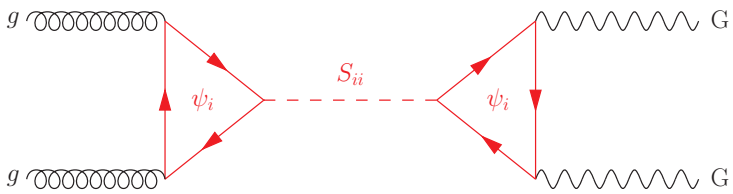

Figure 19. Production via gluon fusion and decay of the scalar resonance S in the asymptotically safe SM extension (3.7). Here, i denotes the BSM flavor index and GG stands for any combination of SM gauge bosons (5.8).

5.4 Diboson spectra and resonances

Consider the situation where the BSM scalars are lighter than twice the mass of the fermions and can be resonantly produced,

$$M_S < 2M_\psi\,, \quad \text{and} \quad M_S < \sqrt{s}\,. \tag{5.7}$$

In such a case the scalars cannot decay on-shell to any of the BSM fermions and because its mixing with the SM Higgs boson is negligible, the only possible decay channels are loop-mediated decays into pairs of gauge bosons

$$GG = gg\,,\ \gamma\gamma\,,\ ZZ\,,\ Z\gamma\,,\ \text{or}\ WW\,. \tag{5.8}$$

The cross sections for these, as well as their relative strengths, depend directly on transformation properties of the BSM fermions under $\mathrm{SU}(3)_C$ and $\mathrm{SU}(2)_L$. Since S does not couple directly to the SM fermions its dominant production mechanism is gluon fusion which proceeds through the loops containing ψ_i. This process is schematically depicted in figure 19. Due to the particular flavor structure of the asymptotically safe BSM sector, one needs to consider a simultaneous production of N_F^2 scalars S_{ij}, each of them coupled to exactly one fermion pair $\bar{\psi}_i\psi_j$. However, since flavor is conserved in the fermion-gauge boson interactions, only diagonal couplings are allowed in this process and the number of simultaneously produced scalars is reduced to N_F. Due to interference effects between the N_F diagrams, it is useful to investigate separately the limiting cases of maximal and no interference.

Maximum interference. Provided that all scalars S_{ii} have the same mass M_S and total decay width Γ_S, the interference between them is maximal and the cross section for a diboson signal GG (5.8) is given by [38, 39]

$$\sigma(pp \to S_{1,\dots,N_F} \to GG) = N_F^2\,\sigma(pp \to S_1)\,\mathrm{BR}(S_1 \to GG) = \frac{N_F^2\,\pi^2}{8M_S^3\,\Gamma_S} I_{\mathrm{pdf}}\,\Gamma^1_{GG}\,\Gamma^1_{gg}\,. \tag{5.9}$$

Notice that (5.9) scales as N_F^2 times the cross section for one individual flavor. In the above, Γ^1_{GG} denotes the partial decay width into two gauge bosons with only one generation of BSM fermions in the loop. Similarly, Γ^1_{gg} stands for the corresponding partial width into two gluons, and I_{pdf} is the integral of parton (gluon) distribution function in proton, evaluated at the energy scale $\mu = M_S$ with the center of mass energy $\sqrt{s}$.

JHEP08(2017)004

No interference. Interference effects are absent provided that the masses of the scalars S_{ii} are narrowly spaced with mass differences ΔM below the detector mass resolution $\Gamma_{\rm det}$, and provided that individual widths do not overlap. Consequently, the production cross section becomes

$$\sigma(pp \to S_{1,\ldots,N_F} \to GG) = N_F\, \sigma(pp \to S_1)\, {\rm BR}(S_1 \to GG) = \frac{N_F \pi^2}{8 M_S^3 \Gamma_{\rm det}}\, I_{\rm pdf}\, \Gamma^1_{GG}\, \Gamma^1_{gg}\,. \tag{5.10}$$

Notice that the total cross section scales as N_F times the cross section for one individual flavor. As such, the absence of interference effects reduces the total cross section parametrically by a factor of N_F over (5.9). We expect that settings with partial interference effects are well covered within the limits (5.9) and (5.10).

The relevant energy scale in the process is $\mu \sim M_S$, that is, the diboson invariant mass. The matching scale M is of the order M_ψ. For M_S below M, roughly $M_S \lesssim M_\psi$ ("low M_S"), the gauge couplings assume SM evolution. For M_S above M ("high M_S"), the gauge couplings follow the BSM fixed-point trajectory. The kinematical range for the high M_S scenario is

$$M_\psi \lesssim M_S \leq 2 M_\psi\,. \tag{5.11}$$

Since characteristic diboson signatures can arise in many BSM scenarios, they have been intensively searched for at the LHC.

Recently both ATLAS and CMS updated their 95% C.L. limits on the fiducial cross section times branching ratio ($\sigma \times BR\times$ acceptance A for a dijet analysis) for a general scalar resonance decaying into gg [40, 41] (updating [42–44]), $Z\gamma$ [45, 46], ZZ [47, 48], WW [49, 50] and $\gamma\gamma$ [51, 52]. The exact limit in each case depends on the mass of the resonance, as well as on its total width. In the following we choose $M_S = 1.5\,$TeV unless otherwise stated, and $\Gamma_S \leq \Gamma_{\rm det}$. First we consider limits on $\sigma(pp \to GG)$ provided by dijet searches. The partial width of S into gluons [53] reads

$$\Gamma_{gg} = \frac{\alpha_s^2 M_S^3}{32\pi^3} \left| \frac{y S_2(R_3) d(R_2)}{M_\psi} A_{1/2}(x) \right|^2, \tag{5.12}$$

where $\alpha_s = 4\pi\alpha_3$ and the loop function is defined as $A_{1/2}(x) = \frac{2}{x^2}[x + (x-1)\arcsin(\sqrt{x})^2]$ and $x = M_S^2/(4M_\psi^2)$. In figure 20 we show $\sigma(pp \to S \to gg)$ versus the mass of the BSM fermions M_ψ for $M_S = 1.5\,$TeV. Solid curves correspond to the limit of maximal interference, while dashed ones refer to no interference. In the latter case the total width is assumed to be $\Gamma_{\rm det} = 0.02 M_S$, while in the former we calculate $\Gamma_S = \sum_{GG} \Gamma_{GG} \simeq \Gamma_{gg}$, which is below $\Gamma_{\rm det}$. Moreover, benchmark B ($R_3 = \mathbf{10}$, $R_2 = \mathbf{1}$, $N_F = 30$, thick blue lines) is contrasted with benchmark D ($R_3 = \mathbf{3}$, $R_2 = \mathbf{4}$, $N_F = 290$, thin green lines) in figure 20. The upper and lower horizontal dashed line indicates the ATLAS 95% C.L. dijet limit for an acceptance $A = 50\%$ and 100%, respectively. We use the NNLO parton distribution functions MSTW2008NNLO [54] with $I_{\rm pdf} = 0.5$ at 13 TeV.

For maximal interference the non-observation of an excess in the dijet mass distribution puts very strong bounds on the mass of the BSM fermions, $M_\psi \gtrsim 87\,(62)\,$TeV for benchmark D and $M_\psi \gtrsim 125\,(89)\,$TeV for benchmark B using $A = 100\%\,(50\%)$. The bounds

JHEP08(2017)004

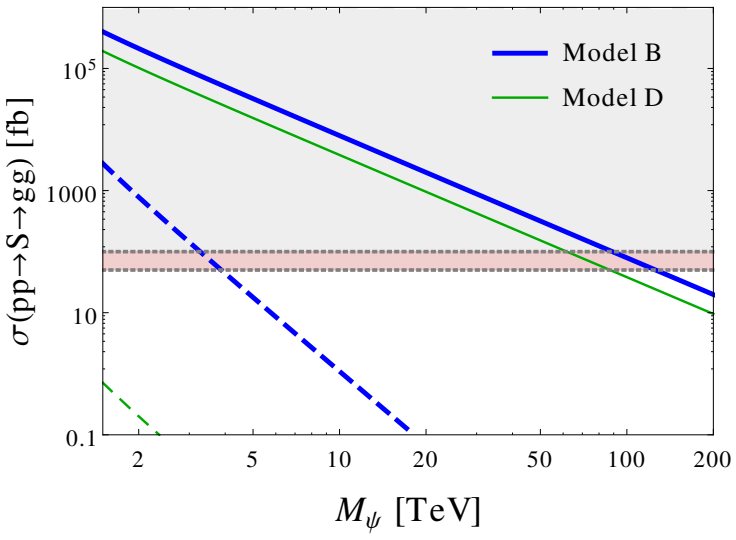

Figure 20. Dijet cross section as a function of the BSM fermion mass M_ψ for benchmark B (thick blue curves), and benchmark D (thin green curves) for $M_S = 1.5\,\text{TeV}$. Solid curves correspond to the maximal interference between N_F scalars, while dashed ones to no interference. The upper and lower horizontal dashed line denotes the ATLAS 95% C.L. limit [40] on the dijet cross section assuming 50% and 100% acceptance, respectively.

gradually become weaker when the interference decreases. In the limit of no interference, the respective lower limits drop to $M_\psi \gtrsim 3.9\,(3.2)\,\text{TeV}$ for benchmark B. For benchmark D the bounds drop below the ones from R-hadron searches given in table 8. Depending on N_F, the two limiting cases may differ by several orders of magnitude. Moreover, since $\Gamma_{gg} \ll \Gamma_{\text{det}}$, the cross section $pp \to S \to gg$ without interference is additionally reduced relative to the maximal one. We conclude that, whenever applicable (5.7), the dijet searches can provide significantly stronger limits on the BSM fermion mass M_ψ than the DY and R-hadron limits worked out in section 5.2 and section 5.3, respectively.

In figure 21 we present exclusion limits in the $M_S - M_\psi$ plane from R-hadron searches (green horizontal stripe) and the dijet cross section limit from ATLAS 95% C.L. — exemplarily for the benchmark B ($R_3 = \mathbf{10}$, $R_2 = \mathbf{1}$, $N_F = 30$) —, also comparing settings with maximal interference (red solid line) and no interference (red dashed line) and $A = 100\%$. Moreover, solid and dashed black lines represent the borders of (5.11) where $M_S = 2M_\psi$ and $M_S = M_\psi$, respectively. The excluded areas are below the solid black lines and to the left and below the red lines. The dark and light blue areas indicate, respectively, the searchable parameter space (5.7) at the LHC (with $\sqrt{s} = 14\,\text{TeV}$) and at future colliders [23]. For masses within the range (5.11) — corresponding to the band between the full and dashed black lines —, the strong coupling α_s is already of non-SM type and enhanced, $\alpha_s(M_S) \gtrsim \alpha_s(M_\psi)$. This regime allows to probe higher values of M_S.

If the BSM fermions transform non-trivially under $\text{SU}(2)_L$, two additional effects arise. Firstly, the lower dijet bound on the fermion mass increases since the cross section $\sigma(pp \to S \to gg)$ scales with $d(R_2)$. Secondly, decays into electroweak gauge bosons

JHEP08(2017)004

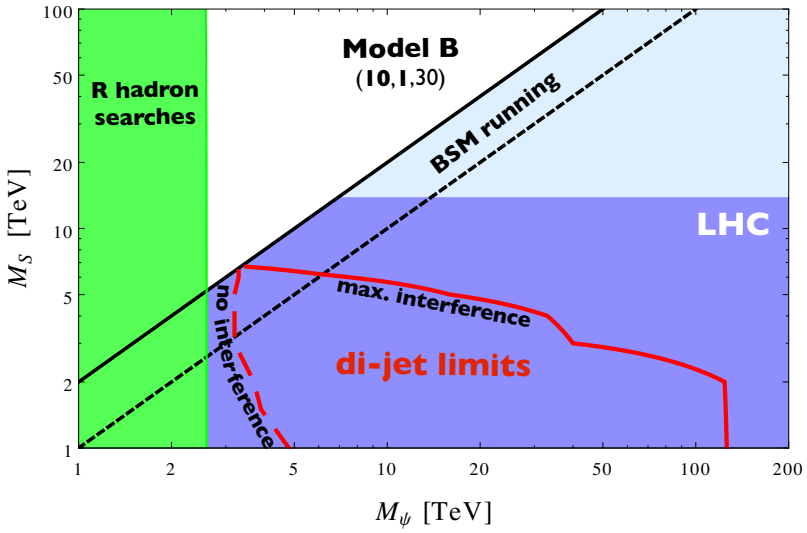

Figure 21. Excluded regions in the $M_\psi - M_S$ plane combining R-hadron searches (green horizontal stripe) with dijet cross section limits from ATLAS 95% C.L. [40] for the benchmark B ($R_3 = \mathbf{10}$, $R_2 = \mathbf{1}$, $N_F = 30$). Excluded regions are also given for the limiting cases of maximal interference (below red solid curve) and no interference (left of red dashed curve), with $A = 100\%$. The dark (light) blue area indicates the searchable parameter space (5.7) at the LHC (future colliders). The strip (5.11) with $M_\psi \lesssim M_S < 2M_\psi$ where an enhancement of α_s due to asymptotically safe running takes place corresponds to the region between the full and dashed black lines.

$VV = \gamma\gamma, WW, ZZ, Z\gamma$ become possible. In order to discuss decays into weak gauge bosons in more detail, it is convenient to introduce the reduced decay widths

$$\bar{\Gamma}_{VV} = \frac{1}{F}\frac{\Gamma_{VV}}{\Gamma_{gg}}, \quad \text{with} \quad F = \left(\frac{4}{3}\frac{C_2(R_2)}{C_2(R_3)}\right)^2, \tag{5.13}$$

which expresses the widths Γ_{VV} in units of Γ_{gg} together with a group theoretical factor F which takes into account the quadratic Casimirs of the BSM fermions. In terms of (5.13), we find

$$\bar{\Gamma}_{WW} = \frac{\alpha_2^2}{\alpha_3^2}, \quad \bar{\Gamma}_{ZZ} = \frac{\alpha_2^4}{2(\alpha_1+\alpha_2)^2\,\alpha_3^2}, \quad \bar{\Gamma}_{Z\gamma} = \frac{\alpha_1\,\alpha_2^3}{(\alpha_1+\alpha_2)^2\,\alpha_3^2}, \quad \bar{\Gamma}_{\gamma\gamma} = \frac{\alpha_1^2\,\alpha_2^2}{2(\alpha_1+\alpha_2)^2\,\alpha_3^2}, \tag{5.14}$$

where $\alpha_1 = g_Y^2/(4\pi)^2$ is the hypercharge coupling. The reduced decay widths depend, in general, on the three gauge couplings. We note that $\bar{\Gamma}_{WW}$ stands out in that it is independent of α_1, and only sensitive to the ratio of the other two gauge couplings.

For low M_S below the matching scale the ratios $\bar{\Gamma}_{VV}$ are solely determined by the SM gauge couplings. In this case F can be determined from any of the VV modes, providing information about R_2 and R_3. Measuring more than one mode serves as a consistency check. In figure 22 we show the ratios Γ_{WW}/Γ_{gg} (blue), Γ_{ZZ}/Γ_{gg} (green), $\Gamma_{Z\gamma}/\Gamma_{gg}$ (red), and $\Gamma_{\gamma\gamma}/\Gamma_{gg}$ (orange), depending on $d(R_2)$ for $R_3 = \mathbf{10}$ (left panel) and $R_3 = \mathbf{3}$ (right panel) for low M_S. The hierarchies among the different modes are fixed in this regime. Deviations can arise from switching on hypercharges of the fermions, or from running

JHEP08(2017)004

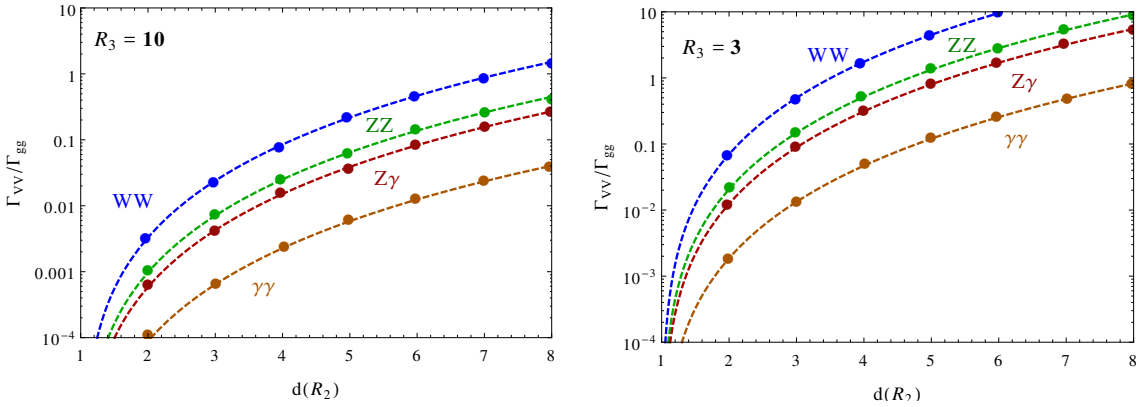

Figure 22. The ratios Γ_{WW}/Γ_{gg} (blue), Γ_{ZZ}/Γ_{gg} (green), $\Gamma_{Z\gamma}/\Gamma_{gg}$ (red), and $\Gamma_{\gamma\gamma}/\Gamma_{gg}$ (orange) versus $d(R_2)$ for $R_3 = \mathbf{10}$ (left) and $R_3 = \mathbf{3}$ (right) for low M_S (see main text).

above the matching scale, at high M_S, where the gauge couplings experience BSM running. This modifies the running of α_2 and α_3 whereas the running of α_1 remains SM-like. We may neglect its slow logarithmic running and can take α_1 as constant for the following considerations.

To discuss further BSM effects, we simplify (5.14) by exploiting that $(\alpha_1/\alpha_2)^2 \lesssim 0.08$ at TeV energies below the matching scale. We find

$$\bar{\Gamma}_{WW} = \frac{\alpha_2^2}{\alpha_3^2}\,, \qquad \bar{\Gamma}_{ZZ} \approx \frac{1}{2}\frac{\alpha_2^2}{\alpha_3^2}\,, \qquad \bar{\Gamma}_{Z\gamma} \approx \frac{\alpha_1}{\alpha_3}\frac{\alpha_2}{\alpha_3}\,, \qquad \bar{\Gamma}_{\gamma\gamma} \approx \frac{1}{2}\frac{\alpha_1^2}{\alpha_3^2}\,, \tag{5.15}$$

where "$\approx$" means equality up to relative corrections of order $\mathcal{O}(\alpha_1^2/\alpha_2^2)$. We observe that $\bar{\Gamma}_{\gamma\gamma}$ is no longer sensitive to α_2 as it has reduced to a ratio of the other two gauge couplings, similarly to $\bar{\Gamma}_{WW}$. It follows that $\bar{\Gamma}_{ZZ} \propto \bar{\Gamma}_{WW}$ and that $\bar{\Gamma}_{Z\gamma} \propto (\bar{\Gamma}_{ZZ} \cdot \bar{\Gamma}_{\gamma\gamma})^{1/2}$.

For models with fully interacting fixed points FP_4 we recall that the weak and strong gauge couplings start growing with RG scale above the matching scale, dictated by the underlying separatrix into the UV fixed point, see figure 12. Their ratio increases from $\alpha_2/\alpha_3 < 1$ below the matching scale to $\alpha_2/\alpha_3 \to 3/2$ sufficiently above the matching scale, invariably inverting the SM hierarchy. In particular, we have that $\alpha_2(\mu)/\alpha_3(\mu) > \alpha_2(M)/\alpha_3(M)$ for $\mu > M$ which implies that both $\bar{\Gamma}_{WW}$ and $\bar{\Gamma}_{ZZ}$ increase accordingly with increasing $\mu > M$. On the other hand $\bar{\Gamma}_{\gamma\gamma}$ becomes suppressed. For $\bar{\Gamma}_{Z\gamma}$, the situation is ambiguous: the growth of $\bar{\Gamma}_{ZZ}$ competes with the suppression of $\bar{\Gamma}_{\gamma\gamma}$ and the outcome in the cross-over region will be model-dependent. Quantitatively, for the fully interacting fixed points of benchmark D (benchmark E) we find that both $\bar{\Gamma}_{WW}$ and $\bar{\Gamma}_{ZZ}$ grow from $\mu = M$ to $\mu = 2M$ by factors of about 12 (3), and that $\bar{\Gamma}_{\gamma\gamma}$ is suppressed by factors of about 13 (2). $\bar{\Gamma}_{Z\gamma}$ is very mildly suppressed only.

For models with partially interacting fixed points FP_2 we generically observe $\alpha_2(\mu > M) > \alpha_2(M)$ and $\alpha_3(\mu > M) < \alpha_3(M)$, e.g. figure 6. This implies that all reduced decay widths increase with increasing $\mu > M$, albeit with different factors, see (5.15). Conversely, for models with FP_3 we have $\alpha_3(\mu > M) > \alpha_3(M)$ and $\alpha_2(\mu > M) < \alpha_2(M)$. As can be

JHEP08(2017)004

deduced from the explicit expressions in (5.14) and (5.15), all four reduced decay widths decrease relative to figure 22.

We conclude that diboson searches involving pairs of electroweak gauge bosons can provide stronger limits than the dijet ones if $d(R_2)$ is sufficiently large. Due to the a priori unknown hierarchy between M_S and M_ψ, correlations of VV with dijet limits cannot be interpreted unambigously. On the other hand, an observation of a GG-resonance determines M_S, while a breakdown of SM-running of α_3, perhaps together with a similar effect in the weak coupling, determines M_ψ. In these cases, extracting F is feasible at low M_S.

Resonance-induced diboson signatures can arise as well from decays of $(\psi\bar{\psi})$-bound states, which are expected to form somewhat below center-of mass energies of $2M_\psi$ for $R_3 \neq \mathbf{1}$ [55]. In our model such ψ-onia can start at about $2M_\psi \gtrsim 3\,\text{TeV}$, which is within LHC limits [56]. Relative decay widths are as in the case of the decays of the scalar S resonance (5.14). Further analysis is beyond the scope of this work.

6 Summary

The concept of an interacting UV fixed point in quantum field theory is of high interest per se; for particle physics it opens up "theory space" for model building. Here, we have investigated asymptotically safe extensions of the Standard Model by adding new fermions and scalar singlet fields. The new matter fields also interact, minimally, via a single Yukawa coupling to help generate interacting UV fixed points. A large variety of stable high energy fixed points emerges where either the strong, or the weak, or both couplings assume finite values, see figures 2, 4. Those where one of the gauge couplings remains asymptotically free can flow into the Standard Model at any scale above $\mathcal{O}(1\text{–}2)\,\text{TeV}$, modulo nearby competing fixed points. Many of the fully interacting fixed points can also be matched onto the Standard Model including at TeV scales, figure 14. Specifically, with fermions charged under $\text{SU}(3)_C \times \text{SU}(2)_L$, we found that they must carry representations higher than the fundamental in at least one of the gauge sectors, figure 4. Also, fully interacting fixed points cannot arise if the fermions are charged under $\text{SU}(2)_L$ only. An intriguing feature of models with fully interacting UV fixed points is a relation between gauge couplings, dictated by asymptotic safety. The number of fundamentally free parameters is thereby reduced offering an enhanced degree of predictivity compared to the Standard Model, quite similar to the idea of unification. Our results have been obtained at two loop accuracy where couplings remain small for all scales, though not parametrically small such as in the Veneziano limit [12]. Of course, further study is needed to explore the full potential of this new direction.

There are several opportunities to look for asymptotically safe BSM physics at colliders. The presence of a large number of new fermionic degrees of freedom from higher representations of $\text{SU}(3)_C \times \text{SU}(2)_L$ with large multiplicities implies striking new physics at the corresponding mass despite being weakly coupled, e.g. figures 6–13. Irrespective of the choice of benchmark models, the qualitative features from the model ansatz laid out in section 3 are rather generic. For low scale matching BSM physics can be just around the corner, as close as $\mathcal{O}(1\text{–}2)\,\text{TeV}$: R-hadron signals arise and the strong coupling

JHEP08(2017)004

evolution itself is altered and further collider tests should be pursued, see figure 16. For $\mathrm{SU}(2)_L$-charged fermions the weak interaction is modified, schematically shown in figure 17. Corresponding shifts in electroweak observables, including WW-production appear above threshold. Loop-induced diboson spectra involving the scalar resonance figure 19 are sensitive to about an order of magnitude higher scales figure 21. While the actual limits are rather model-dependent, this demonstrates that the phenomenology of asymptotically safe BSM can be probed at the LHC at Run 2 and beyond. Tests of the weak interaction are also encouraged at high energy e^+e^- colliders [23–25].

Acknowledgments

We thank Joachim Brod, John Donoghue, Veronica Sanz, Martin Schmaltz, and Enrico Sessolo for useful discussions. AB is grateful to the Physics Department at Boston University for its hospitality and stimulating environment while this project was pursued. AB is supported by an STFC studentship, GH and KK in part by the DFG Research Unit FOR 1873 "Quark Flavor Physics and Effective Field Theories", and DL by the Science and Technology Facilities Council (STFC) under grant number ST/L000504/1.

A Technicalities

The appendix summarises group theoretical formulæ and loop coefficients, together with a discussion of UV-IR connecting separatrices.

Loop coefficients and group theoretical factors. We summarise formulæ for perturbative loop coefficients. We have exploited general expressions as given in [18–21]. We consider the SM matter fields, together with N_F vector BSM fermions in the R_3 and R_2 representation under $\mathrm{SU}(3)_C$ and $\mathrm{SU}(2)_L$, respectively. The beta functions are stated in (3.7). We reproduce them here for completeness,

$$\begin{aligned}\beta_3 &= (-B_3 + C_3\,\alpha_3 + G_3\,\alpha_2 - D_3\,\alpha_y)\,\alpha_3^2\,,\\ \beta_2 &= (-B_2 + C_2\,\alpha_2 + G_2\,\alpha_3 - D_2\,\alpha_y)\,\alpha_2^2\,,\\ \beta_y &= (E\,\alpha_y - F_2\,\alpha_2 - F_3\,\alpha_3)\,\alpha_y\,.\end{aligned} \tag{A.1}$$

The gauge one loop coefficients read

$$\begin{aligned}B_3 &= 14 - \frac{8}{3}N_F\,S_2(R_3)\,d(R_2)\,,\\ B_2 &= \frac{19}{3} - \frac{8}{3}N_F\,S_2(R_2)\,d(R_3)\,.\end{aligned} \tag{A.2}$$

At two loop level for the gauge couplings we have the "diagonal" gauge contributions

$$\begin{aligned}C_3 &= -52 + 4N_F\,S_2(R_3)\,d(R_2)\big(2C_2(R_3) + 10\big)\,,\\ C_2 &= \frac{35}{3} + 4N_F\,S_2(R_2)\,d(R_3)\left(2C_2(R_2) + \frac{20}{3}\right)\,,\end{aligned} \tag{A.3}$$

JHEP08(2017)004

together with the "mixing" gauge contributions

$$\begin{aligned} G_3 &= 9 + 8N_F\, S_2(R_3)\, C_2(R_2)\, d(R_2)\,, \\ G_2 &= 24 + 8N_F\, S_2(R_2)\, C_2(R_3)\, d(R_3)\,. \end{aligned} \tag{A.4}$$

Furthermore, the BSM Yukawa couplings also contribute at two loop level to the running of the gauge couplings with coefficients

$$\begin{aligned} D_3 &= 4N_F^2\, S_2(R_3)\, d(R_2)\,, \\ D_2 &= 4N_F^2\, S_2(R_2)\, d(R_3)\,. \end{aligned} \tag{A.5}$$

The running of the BSM Yukawa coupling receives one loop contributions from itself as well as from the gauge couplings with coefficients

$$\begin{aligned} E &= 2[N_F + d(R_2)\, d(R_3)]\,, \\ F_3 &= 12C_2(R_3)\,, \\ F_2 &= 12C_2(R_2)\,. \end{aligned} \tag{A.6}$$

In the above expressions, $C_2(R)$, $S_2(R)$ and $d(R)$ denote the quadratic Casimir invariant, the Dynkin index and dimension of the representation R, respectively. They are related by

$$S_2(R) = d(R)\, C_2(R)/d(\mathrm{Adj})\,, \tag{A.7}$$

to the dimension of the adjoint representation $d(\mathrm{Adj})$. It is also convenient to parametrize the loop coefficients through the weights (p, q) for irreducible SU(3) representations R_3, and, similarly, through the highest weight ℓ for SU(2) representations R_2,

$$\begin{aligned} d(R_3) &= \frac{1}{2}(p+1)(q+1)(p+q+2)\,, & & \\ C_2(R_3) &= p + q + \frac{1}{3}(p^2+q^2+pq)\,, & \text{with} \quad & p, q = 0, 1\cdots\,, \\ d(R_2) &= 2\ell + 1\,, & & \\ C_2(R_2) &= \ell(\ell+1)\,, & \text{with} \quad & \ell = 0, \frac{1}{2}, 1\cdots\,. \end{aligned} \tag{A.8}$$

Evidently, in the absence of BSM matter fields ($N_F = 0$), the perturbative loop coefficients reduce to their SM values

$$\begin{aligned} B_3^{\mathrm{SM}} &= 14\,, & B_2^{\mathrm{SM}} &= 19/3\,, \\ C_3^{\mathrm{SM}} &= -52\,, & C_2^{\mathrm{SM}} &= 35/3\,, \\ G_3^{\mathrm{SM}} &= 9\,, & G_2^{\mathrm{SM}} &= 24\,, \end{aligned} \tag{A.9}$$

together with $E^{\mathrm{SM}} = F_2^{\mathrm{SM}} = F_3^{\mathrm{SM}} = 0$. In this limit and at two loop accuracy, we observe that the $\mathrm{SU}(2)_L$ sector displays a "would-be" Banks-Zaks type IR fixed point at

$$(\alpha_2^*, \alpha_3^*) = \left(\frac{19}{35}, 0\right). \tag{A.10}$$

JHEP08(2017)004

The $\mathrm{SU}(3)_C$ sector does not display signs of a Banks-Zaks type fixed point owing to $B_3/C_3 < 0$. Fingerprints of (A.10) become visible for scenarios with BSM matter uncharged under $\mathrm{SU}(2)_L$.

At places, primed two loop coefficients arise. They relate to their unprimed counterparts as

$$\begin{aligned} C_3' &= C_3 - D_3\, F_3/E\,, \\ C_2' &= C_2 - D_2\, F_2/E\,, \\ G_3' &= G_3 - D_3\, F_2/E\,, \\ G_2' &= G_2 - D_2\, F_3/E\,. \end{aligned} \tag{A.11}$$

In the gauge beta functions, the primed terms arise as shifts of the unprimed coefficients induced by the BSM Yukawa coupling which takes a fixed point proportional to the gauge couplings.

UV-IR connecting separatrices. Next, we summarise formulæ and results related to the running of couplings along UV safe trajectories emanating out of an interacting UV fixed point. We are particularly interested in the running of the relevant gauge coupling along the UV-IR connecting hypercritical surface down to energy scales μ close to the mass M of the new matter fields, $\mu \approx M$, where the model connects with the SM. We approximate the beta functions (A.1) as

$$\begin{aligned} \partial_t \alpha &= \alpha^2(-B + C\,\alpha - D\alpha_y)\,, \\ \partial_t \alpha_y &= \alpha_y(E\alpha_y - F\alpha)\,. \end{aligned} \tag{A.12}$$

These equations are applicable for partially interacting fixed points where one of the gauge couplings becomes asymptotically safe and the other one asymptotically free. The contribution of the latter is neglected. Quantitatively, corrections from the asymptotically free coupling are subleading in the UV and numerically small for the models discussed here. The coefficients B, C, D and F then take the values corresponding to the asymptotically safe gauge coupling. To find the exact UV-IR connecting separatrix, the system (A.12) must be solved numerically. However, for most cases of interest, approximate estimates can be obtained as well. We discuss two strategies.

UV critical surface approximation. Firstly, we may approximate α_y along the separatrix through its values along the UV critical surface. The virtue of this approximation is that it becomes sufficiently exact close to the UV fixed point. Quantitatively, on the UV hypercritical surface, the BSM Yukawa coupling is determined via the gauge coupling as

$$\alpha_y = C_y\,(\alpha - \alpha^*) + \alpha_y^*\,. \tag{A.13}$$

In this expression, C_y is defined via the relevant eigendirection at the UV fixed point, with $(1, C_y)^T$ denoting the eigenvector with negative eigenvalue of the stability matrix M at the fixed point in the basis $(\alpha, \alpha_y)^T$. In terms of the perturbative loop coefficients, it reads

$$C_y = 2\frac{F}{E}\left(1 + \sqrt{1 - \frac{2BF(C^2E^2 - 3CDEF + 2D^2F^2) - B^2C^2E^2}{F^2(DF - CE)^2}} + \frac{BCE}{F(DF - CE)}\right)^{-1}. \tag{A.14}$$

JHEP08(2017)004

In order to map out the UV-IR connecting separatrix we insert (A.13) into (A.12) to find

$$\partial_t \alpha = \alpha^2(-\tilde{B} + \tilde{C}\,\alpha)\,, \tag{A.15}$$

with

$$\begin{aligned} \tilde{B} &= B + D(\alpha_y^* - C_y \alpha^*)\,, \\ \tilde{C} &= C - D\,C_y\,. \end{aligned} \tag{A.16}$$

Solving the RG flow (A.15) analytically, we find $\alpha(\mu)$ at any RG scale μ in terms of $\alpha(M)$ determined at some reference mass scale M,

$$\left(\frac{\mu}{M}\right)^{-\vartheta} = \frac{\alpha^* - \alpha(M)}{\alpha^* - \alpha(\mu)} \frac{\alpha(\mu)}{\alpha(M)} \exp\left(\frac{\alpha^*}{\alpha(M)} - \frac{\alpha^*}{\alpha(\mu)}\right). \tag{A.17}$$

Furthermore, the UV relevant scaling exponent ϑ is given by

$$\vartheta = \tilde{B}^2/\tilde{C} < 0 \tag{A.18}$$

in terms of (A.16). The result (A.17) can be resolved for $\alpha(\mu)$ with the help of the Lambert function,

$$\alpha(\mu) = \frac{\alpha_*}{1 + W(\mu, M, \vartheta)}\,, \tag{A.19}$$

where $W(\mu, M, \vartheta) \equiv W_L[z(\mu, M, \vartheta)]$ with $W_L[z]$ denoting the Lambert function, defined implicitly through $z = W_L \exp W_L$. The variable $z(\mu, M, \vartheta)$ is given explicitly by

$$z(\mu, M, \vartheta) = \left(\frac{\mu}{M}\right)^{\vartheta} \left(\frac{\alpha^*}{\alpha_M} - 1\right) \exp\left(\frac{\alpha^*}{\alpha_M} - 1\right), \tag{A.20}$$

with the relevant scaling exponent ϑ given in (A.18). For any value of $\alpha_M \equiv \alpha(\mu = M) > 0$ there is a unique branch of the Lambert function connecting $\alpha(\mu)$ inbetween α_M and α^*. The expression (A.19) can now be used to approximately determine the mass scale M by matching it to values of the SM.

Yukawa nullcline approximation. Alternatively, we may use the Yukawa nullcline to estimate α_y along the UV-IR connecting separatrix. In the system (A.12), the Yukawa nullcline is given by

$$\alpha_y = \frac{F}{E}\,\alpha\,. \tag{A.21}$$

The virtue of using (A.21) to approximate the separatrix is twofold. Firstly, close to the Gaussian fixed point, the UV-IR connecting separatrix and the nullcline coincide, meaning that (A.21) is a very good approximation if the gauge coupling is matched to the SM at scales where $\alpha \ll \alpha^*$. Secondly, rewriting (A.21) as

$$\alpha_y = \frac{F}{E}(\alpha - \alpha^*) + \alpha_y^*\,, \tag{A.22}$$

we conclude that the nullcline also coincides with the hypercritical surface at the UV fixed point. Hence, (A.21) can be viewed as a "global linear approximation" for the UV-IR connecting separatrix. Comparing this approximation with the UV hypercritical surface (A.13) in the limit $B/C' \ll 1$ (with $C' = C - DF/E$), we observe that (A.14) becomes

JHEP08(2017)004

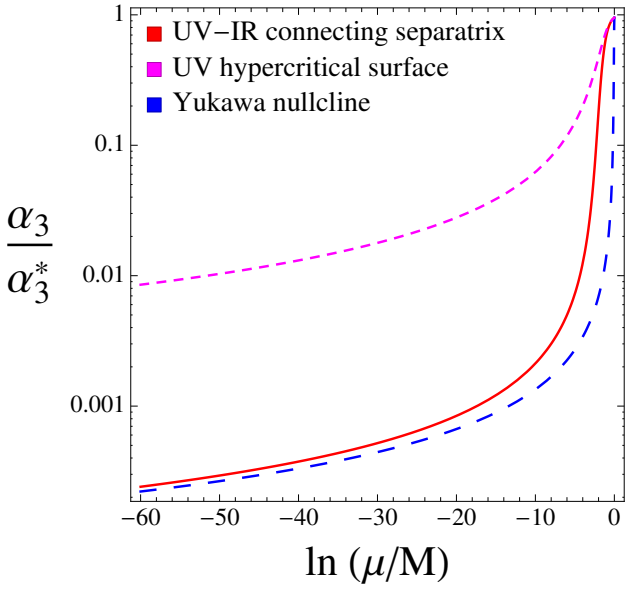

Figure 23. UV-IR connecting trajectories at the example of a partially interacting fixed point FP_3 and parameters $R_2 = \mathbf{1}$, $R_3 = \mathbf{10}$, $N_F = 30$, showing the exact separatrix (red line) in comparison with the UV hypercritical surface approximation (magenta), (A.13), and the Yukawa nullcline approximation (blue), (A.22). The Yukawa nullcline offers a good global approximation for the exact UV-IR connecting separatrix.

$C_y = F/E + \mathcal{O}(B/C')$, establishing that the hypercritical surface (A.22) exactly coincides with the Yukawa nullcline. For finite $B/C' < 1$, however, the slopes of the hypercritical surface and the nullcline differ. Inserting (A.21) into the running of the gauge coupling (A.12) we find

$$\partial_t \alpha = \alpha^2(-B + C'\,\alpha)\,. \tag{A.23}$$

The analytical solution to (A.23) with initial condition $\alpha(\mu = M) = \alpha_M$ is given by (A.19) with (A.20), the sole difference being the value for the parameter ϑ which now reads

$$\vartheta = B^2/C' < 0 \tag{A.24}$$

instead of (A.18).

Quantitatively, our results are illustrated in figure 23 at the example of a partially interacting fixed point FP_3 with $R_2 = \mathbf{1}$, $R_3 = \mathbf{10}$, $N_F = 30$. We compare the exact numerical solution for $\alpha_3(\mu)$ (full red line) with the hypercritical surface approximation (magenta) and with the Yukawa nullcline approximation (blue). We observe that the UV region (IR region) is well-approximated by the UV critical surface (Yukawa nullcline), respectively. We also observe that the exact separatrix is globally well approximated by the Yukawa nullcline, corresponding to (A.19) together with (A.20) and (A.24). This approximation offers good quantitative estimates for the matching scale M.

Throughout the main body, we have used the exact numerical separatrix for our results. We have also confirmed that the critical surface and the nullcline approximations offer very good accuracy in their respective domains of applicability.

JHEP08(2017)004

References

[1] D.J. Gross and F. Wilczek, *Ultraviolet behavior of non-Abelian gauge theories*, *Phys. Rev. Lett.* **30** (1973) 1343 [INSPIRE].

[2] H.D. Politzer, *Reliable perturbative results for strong interactions?*, *Phys. Rev. Lett.* **30** (1973) 1346 [INSPIRE].

[3] S.R. Coleman and D.J. Gross, *Price of asymptotic freedom*, *Phys. Rev. Lett.* **31** (1973) 851 [INSPIRE].

[4] N.-P. Chang, *Eigenvalue conditions and asymptotic freedom for Higgs scalar gauge theories*, *Phys. Rev.* **D 10** (1974) 2706 [INSPIRE].

[5] G.F. Giudice, G. Isidori, A. Salvio and A. Strumia, *Softened gravity and the extension of the standard model up to infinite energy*, *JHEP* **02** (2015) 137 [arXiv:1412.2769] [INSPIRE].

[6] B. Holdom, J. Ren and C. Zhang, *Stable Asymptotically Free Extensions (SAFEs) of the standard model*, *JHEP* **03** (2015) 028 [arXiv:1412.5540] [INSPIRE].

[7] G.M. Pelaggi, A. Strumia and S. Vignali, *Totally asymptotically free trinification*, *JHEP* **08** (2015) 130 [arXiv:1507.06848] [INSPIRE].

[8] K.G. Wilson, *Renormalization group and critical phenomena. I. Renormalization group and the Kadanoff scaling picture*, *Phys. Rev.* **B 4** (1971) 3174 [INSPIRE].

[9] S. Weinberg, *Ultraviolet divergences in quantum theories of gravitation*, in *General relativity: an Einstein centenary survey*, S.W. Hawking and W. Israel eds., Cambridge University Press, Cambridge U.K. (1080), pp. 790–831 [INSPIRE].

[10] D.F. Litim, *Renormalisation group and the Planck scale*, *Phil. Trans. Roy. Soc. Lond.* **A 369** (2011) 2759 [arXiv:1102.4624] [INSPIRE].

[11] A.D. Bond and D.F. Litim, *Theorems for asymptotic safety of gauge theories*, *Eur. Phys. J.* **C 77** (2017) 429 [arXiv:1608.00519] [INSPIRE].

[12] D.F. Litim and F. Sannino, *Asymptotic safety guaranteed*, *JHEP* **12** (2014) 178 [arXiv:1406.2337] [INSPIRE].

[13] D.F. Litim, M. Mojaza and F. Sannino, *Vacuum stability of asymptotically safe gauge-Yukawa theories*, *JHEP* **01** (2016) 081 [arXiv:1501.03061] [INSPIRE].

[14] W.E. Caswell, *Asymptotic behavior of non-Abelian gauge theories to two-loop order*, *Phys. Rev. Lett.* **33** (1974) 244 [INSPIRE].

[15] T. Banks and A. Zaks, *On the phase structure of vector-like gauge theories with massless fermions*, *Nucl. Phys.* **B 196** (1982) 189 [INSPIRE].

[16] K. Falls, D.F. Litim, K. Nikolakopoulos and C. Rahmede, *A bootstrap towards asymptotic safety*, arXiv:1301.4191 [INSPIRE].

[17] K. Falls, D.F. Litim, K. Nikolakopoulos and C. Rahmede, *Further evidence for asymptotic safety of quantum gravity*, *Phys. Rev.* **D 93** (2016) 104022 [arXiv:1410.4815] [INSPIRE].

[18] M.E. Machacek and M.T. Vaughn, *Two-loop renormalization group equations in a general quantum field theory. I. Wave function renormalization*, *Nucl. Phys.* **B 222** (1983) 83 [INSPIRE].

JHEP08(2017)004

[19] M.E. Machacek and M.T. Vaughn, *Two-loop renormalization group equations in a general quantum field theory. II. Yukawa couplings*, *Nucl. Phys.* **B 236** (1984) 221 [INSPIRE].

[20] M.E. Machacek and M.T. Vaughn, *Two-loop renormalization group equations in a general quantum field theory. III. Scalar quartic couplings*, *Nucl. Phys.* **B 249** (1985) 70 [INSPIRE].

[21] M.-x. Luo, H.-w. Wang and Y. Xiao, *Two-loop renormalization group equations in general gauge field theories*, *Phys. Rev.* **D 67** (2003) 065019 [hep-ph/0211440] [INSPIRE].

[22] Particle Data Group, C. Patrignani et al., *Review of particle physics*, *Chin. Phys.* **C 40** (2016) 100001 [INSPIRE].

[23] V. Shiltsev, *On the future high energy colliders*, in Proceedings of the *Meeting of the APS Division of Particles and Fields (DPF 2015)*, Ann Arbor U.S.A., 4–8 Aug 2015 [arXiv:1509.08369] [INSPIRE].

[24] TLEP Design Study Working Group, M. Bicer et al., *First look at the physics case of TLEP*, *JHEP* **01** (2014) 164 [arXiv:1308.6176] [INSPIRE].

[25] D. d'Enterria, *Physics at the FCC-ee*, in Proceedings of the *17th Lomonosov Conference on Elementary Particle Physics*, Moscow Russia, 20–26 Aug 2015 [arXiv:1602.05043] [INSPIRE].

[26] CMS collaboration, *Constraints on parton distribution functions and extraction of the strong coupling constant from the inclusive jet cross section in pp collisions at* $\sqrt{s} = 7$ *TeV*, *Eur. Phys. J.* **C 75** (2015) 288 [arXiv:1410.6765] [INSPIRE].

[27] CMS collaboration, *Measurements of differential jet cross sections in proton-proton collisions at* $\sqrt{s} = 7$ *TeV with the CMS detector*, *Phys. Rev.* **D 87** (2013) 112002 [*Erratum ibid.* **D 87** (2013) 119902] [arXiv:1212.6660] [INSPIRE].

[28] CMS collaboration, *Measurement of the inclusive 3-jet production differential cross section in proton-proton collisions at 7 TeV and determination of the strong coupling constant in the TeV range*, *Eur. Phys. J.* **C 75** (2015) 186 [arXiv:1412.1633] [INSPIRE].

[29] DELPHI, OPAL, LEP Electroweak, ALEPH and L3 collaborations, S. Schael et al., *Electroweak measurements in electron-positron collisions at W-boson-pair energies at LEP*, *Phys. Rept.* **532** (2013) 119 [arXiv:1302.3415] [INSPIRE].

[30] ATLAS and CMS collaborations, P. Azzurri, *Results from CMS and ATLAS: electroweak symmetry, breaking and beyond*, PoS(BORMIO2016)044 [INSPIRE].

[31] D.S.M. Alves, J. Galloway, J.T. Ruderman and J.R. Walsh, *Running electroweak couplings as a probe of new physics*, *JHEP* **02** (2015) 007 [arXiv:1410.6810] [INSPIRE].

[32] R. Barbieri, A. Pomarol, R. Rattazzi and A. Strumia, *Electroweak symmetry breaking after LEP-1 and LEP-2*, *Nucl. Phys.* **B 703** (2004) 127 [hep-ph/0405040] [INSPIRE].

[33] G. Cacciapaglia, C. Csáki, G. Marandella and A. Strumia, *The minimal set of electroweak precision parameters*, *Phys. Rev.* **D 74** (2006) 033011 [hep-ph/0604111] [INSPIRE].

[34] M. Farina et al., *Energy helps accuracy: electroweak precision tests at hadron colliders*, *Phys. Lett.* **B 772** (2017) 210 [arXiv:1609.08157] [INSPIRE].

[35] CMS collaboration, *Search for long-lived charged particles in proton-proton collisions at* $\sqrt{s} = 13$ *TeV*, *Phys. Rev.* **D 94** (2016) 112004 [arXiv:1609.08382] [INSPIRE].

[36] ATLAS collaboration, *Search for heavy long-lived charged R-hadrons with the ATLAS detector in 3.2 fb*$^{-1}$ *of proton-proton collision data at* $\sqrt{s} = 13$ *TeV*, *Phys. Lett.* **B 760** (2016) 647 [arXiv:1606.05129] [INSPIRE].

JHEP08(2017)004

[37] CMS collaboration, *Search for heavy stable charged particles with 12.9 fb^{-1} of 2016 data*, CMS-PAS-EXO-16-036 (2016).

[38] J.F. Gunion, H.E. Haber, G.L. Kane and S. Dawson, *The Higgs hunter's guide*, *Front. Phys.* **80** (2000) 1 [INSPIRE].

[39] A. Djouadi, *The anatomy of electro-weak symmetry breaking. II. The Higgs bosons in the minimal supersymmetric model*, *Phys. Rept.* **459** (2008) 1 [hep-ph/0503173] [INSPIRE].

[40] ATLAS collaboration, *Search for new phenomena in dijet events using 37 fb^{-1} of pp collision data collected at $\sqrt{s} = 13$ TeV with the ATLAS detector*, arXiv:1703.09127 [INSPIRE].

[41] CMS collaboration, *Searches for dijet resonances in pp collisions at $\sqrt{s} = 13$ TeV using data collected in 2016*, CMS-PAS-EXO-16-056 (2017).

[42] ATLAS collaboration, *Search for light dijet resonances with the ATLAS detector using a trigger-level analysis in LHC pp collisions at $\sqrt{s} = 13$ TeV*, ATLAS-CONF-2016-030 (2016).

[43] ATLAS collaboration, *Search for new phenomena in dijet events with the ATLAS detector at $\sqrt{s} = 13$ TeV with 2015 and 2016 data*, ATLAS-CONF-2016-069 (2016).

[44] CMS collaboration, *Search for dijet resonances in proton-proton collisions at $\sqrt{s} = 13$ TeV and constraints on dark matter and other models*, *Phys. Lett.* **B 769** (2017) 520 [arXiv:1611.03568] [INSPIRE].

[45] ATLAS collaboration, *Search for heavy resonances decaying to a Z boson and a photon in pp collisions at $\sqrt{s} = 13$ TeV with the ATLAS detector*, ATLAS-CONF-2016-010 (2016).

[46] CMS collaboration, *Search for high-mass resonances in $Z\gamma \to e^+e^-\gamma/\mu^+\mu^-\gamma$ final states in proton-proton collisions at $\sqrt{s} = 13$ TeV*, CMS-PAS-EXO-16-034 (2016).

[47] ATLAS collaboration, *Searches for heavy ZZ and ZW resonances in the $\ell\ell qq$ and $\nu\nu qq$ final states in pp collisions at $\sqrt{s} = 13$ TeV with the ATLAS detector*, ATLAS-CONF-2016-082 (2016).

[48] CMS collaboration, *Search for a heavy scalar boson decaying into a pair of Z bosons in the $2\ell 2\nu$ final state*, CMS-PAS-HIG-16-001 (2016).

[49] ATLAS collaboration, *Search for WW/WZ resonance production in the $\ell\nu qq$ final state at $\sqrt{s} = 13$ TeV with the ATLAS detector at the LHC*, ATLAS-CONF-2015-075 (2015).

[50] ATLAS collaboration, *Search for a high-mass Higgs boson decaying to a pair of W bosons in pp collisions at $\sqrt{s} = 13$ TeV with the ATLAS detector*, ATLAS-CONF-2016-021 (2016).

[51] ATLAS collaboration, *Search for scalar diphoton resonances with 15.4 fb^{-1} of data collected at $\sqrt{s} = 13$ TeV in 2015 and 2016 with the ATLAS detector*, ATLAS-CONF-2016-059 (2016).

[52] CMS collaboration, *Search for high-mass diphoton resonances in proton-proton collisions at 13 TeV and combination with 8 TeV search*, *Phys. Lett.* **B 767** (2017) 147 [arXiv:1609.02507] [INSPIRE].

[53] M. Cvetič, J. Halverson and P. Langacker, *String consistency, heavy exotics and the 750 GeV diphoton excess at the LHC*, *Fortschr. Phys.* **64** (2016) 748 [arXiv:1512.07622] [INSPIRE].

[54] A.D. Martin, W.J. Stirling, R.S. Thorne and G. Watt, *Parton distributions for the LHC*, *Eur. Phys. J.* **C 63** (2009) 189 [arXiv:0901.0002] [INSPIRE].

[55] Y. Kats and M.J. Strassler, *Probing colored particles with photons, leptons and jets*, *JHEP* **11** (2012) 097 [*Erratum ibid.* **07** (2016) 009] [arXiv:1204.1119] [INSPIRE].

[56] Y. Kats and M.J. Strassler, *Resonances from QCD bound states and the 750 GeV diphoton excess*, *JHEP* **05** (2016) 092 [*Erratum ibid.* **07** (2016) 044] [arXiv:1602.08819] [INSPIRE].

JHEP08(2017)004